Smart Materials and
Structures

PURPOSE-LED
PUBLISHING™

PAPER

Characterizing the transduction behavior of ionic polymer-metal composite actuators and sensors via dimensional analysis

To cite this article: Zakai J Olsen and Kwang J Kim 2022 *Smart Mater. Struct.* **31** 025014

View the article online for updates and enhancements.

You may also like

- Analysis and experiment on a self-sensing ionic polymer–metal composite actuator
Doan Ngoc Chi Nam and Kyoung Kwan Ahn

- Modeling and control of a self-sensing polymer metal composite actuator
Doan Ngoc Chi Nam and Kyoung Kwan Ahn

- AI-based hybrid neural network with PID control system for deflection control of IPMC soft actuators in robotic applications
Amitava Das, Vishal Roy, Deepro Sen et al.

This content was downloaded from IP address 131.216.14.8 on 06/04/2026 at 21:46

Smart Mater. Struct. **31** (2022) 025014 (29pp) https://doi.org/10.1088/1361-665X/ac411e

Characterizing the transduction behavior of ionic polymer-metal composite actuators and sensors via dimensional analysis

Zakai J Olsen and Kwang J Kim*

Active Materials and Smart Living (AMSL) Lab, Department of Mechanical Engineering, University of Nevada Las Vegas, Las Vegas, NV, United States of America

E-mail: kwang.kim@unlv.edu

Received 12 October 2021, revised 23 November 2021
Accepted for publication 8 December 2021
Published 24 December 2021

Abstract

Ionic polymer-metal composites (IPMCs) are functional smart materials that exhibit both electromechanical and mechanoelectrical transduction properties, and the physical phenomenon underlying the transduction mechanisms have been studied across the literature extensively. Here we use a new modeling framework to conduct the most comprehensive dimensional analysis of IPMC transduction phenomena, characterizing the IPMC actuator displacement, actuator blocking force, short-circuit sensing current, and open-circuit sensing voltage under static and dynamic loading. The information obtained in this analysis is used to construct nonlinear regression models for the transduction response as univariant and multivariant functions. Automatic differentiation techniques are leveraged to linearize the nonlinear regression models in the vicinity of a typical IPMC description and derive the sensitivity of the transduction response with respect to the driving independent variables. Further, the multiphysics model is validated using experimental data collected for the dynamic IPMC actuator and voltage sensor. With data collected from physical samples of IPMC materials in-lab, the regression models developed under the new computational framework are verified.

Supplementary material for this article is available online

Keywords: soft-robotics, ionic polymer-metal composites, electroactive polymers, dimensional analysis, finite element analysis

(Some figures may appear in colour only in the online journal)

* Author to whom any correspondence should be addressed.

© 2021 IOP Publishing Ltd
All rights, including for text and data mining, AI training, and similar technologies, are reserved.

Nomenclature

Fields, parameters, and operators

Quantity	SI units	Description
c	$\left[\mathrm{mol\ m^{-3}}\right]$	Molar concentration
$\mathcal{C}_i$	$[\square]$	Material modulus (denoted by index set in subscripts)
$\nabla\times$	$\left[\mathrm{m^{-1}}\right]$	Curl operator
$\nabla\cdot$	$[1/m]$	Divergence operator
$\nabla_S\cdot$	$[1/m]$	Surface divergence operator
$\otimes$	$[-]$	Dyadic product
$\mathcal{D}$	$\left[\mathrm{m^2\ s^{-1}}\right]$	Diffusivity
$\mathrm{d}\Omega$	$\left[\mathrm{m^3}\right]$	Differential element of domain
$\mathrm{d}S$	$\left[\mathrm{m^2}\right]$	Differential element of boundary
$\mathrm{d}\ell$	$[\mathrm{m}]$	Differential element of curve/path
Δ	$[-]$	Dimensionless actuation displacement
$\underline{d}$	$\left[\mathrm{C\,m^{-2}}\right]$	Spatial/Material electric displacement
ϵ	$\left[\mathrm{Fm^{-1}}\right]$	Dielectric constant
$\underline{e}$	$\left[\mathrm{Vm^{-1}}\right]$	Electric field
$\underline{\underline{\varepsilon}}$	$[-]$	Infinitesimal strain tensor
$\mathcal{F}$	$\left[\mathrm{Cmol^{-1}}\right]$	Faraday's constant
∇	$[1/m]$	Gradient operator
∇_S	$[1/m]$	Surface gradient operator
$\underline{h}$	$\left[\square\,\mathrm{m\,s^{-1}}\right]$	Flux vector
$I_{sc}, I_{\pm}$	$[\mathrm{A}]$	Short-circuit current, Upper (+)/lower (−) clamp current
$\underline{\underline{I}}$	$[-]$	Identity tensor
k_f	$\left[\mathrm{m^2\,s^{-1}\,Pa}\right]$	Hydraulic permeability
λ	$[-]$	Volume fraction
λ_d	$[\mathrm{m}]$	Debye screening length
n_{dw}, n_{d+}	$[-]$	Water/Ion transference coefficient
ν	$\left[\mathrm{m^3\,mol^{-1}}\right]$	Molar volume of fluid constituent
$\underline{n}$	$[-]$	Surface normal vector
$\Omega_{0,t}, \partial\Omega_{0,t}$	$[-]$	Domain/Domain boundary (Material, Spatial)
$\wp$	$[Pa]$	Conjugate pressure
$\mathcal{P}$	$[Pa]$	Lagrange multiplier (Lagrange pressure)
Π	$[-]$	Dimensionless group
$\underline{\underline{\mathbb{P}}}$	$[-]$	Surface projection tensor
ϕ	$[\mathrm{V}]$	Electric potential
$\phi_{oc}, \phi_{\pm}$	$[\mathrm{V}]$	Open-circuit voltage, Upper (+)/lower (−) clamp potential
R	$\left[\mathrm{J\,mol^{-1}K}\right]$	Universal gas constant
ρ	$\left[\mathrm{kg\,m^{-3}}\right]$	Mass density
r_e^S	$[\Omega\,\mathrm{m}]$	Electrode resistivity
$\underline{\underline{\sigma}}$	$[Pa]$	Cauchy stress tensor (additive components w/subscript)
t	$[\mathrm{s}]$	Time
τ	$[\mathrm{s}]$	Timescale (in dimensional analysis)
T	$[\Theta]$	Thermodynamic temperature
$\underline{t}$	$[\mathrm{Pa}]$	Surface traction vector
$\underline{u}$	$[\mathrm{m}]$	Displacement field
z	$[-]$	Charge number

The notation ‘ $[\square]$’ indicates units depend on particular quantity in question

Subscripts	
a	Applied value (boundary conditions)
c	Characteristic field value (in dimensional analysis)
w	Solvent water species
$+$	Cation species/Upper electrode interface
$-$	Anion species/Lower electrode interface
0	Initial/reference quantity
$\{E, \nu\}$	Material moduli (Young, Poisson)
Superscripts	
T	Transpose (of a tensor/matrix quantity)
Accents/bracket operators	
$\widehat{}$	Dimensionless field variable
$\langle\square\rangle$	Average of argument
$\|\square\|$	Surface jump in argument

1. Introduction

1.1. The ionic polymer-metal composite

Ionic polymer-metal composites (IPMCs) are a class of highly functional smart materials called electroactive polymers (EAP). These materials exhibit a mechanical response to electrical inputs, (electromechanical transduction) and conversely an electrical response to mechanical input, (mechanoelectrical transduction) [1–3]. These energy transduction capabilities allow EAP materials to be used as both actuators (electromechanical), and sensors (mechanoelectrical), and hence find many applications in robotics, soft robotics, wearable technology, and biomimetics. The IPMC in particular shows great promise for the future of robotic engineering and design. These materials demonstrate large deformations in response to low voltage electrical inputs (0.5–2 V), relatively fast response speed (0.1–5 Hz), and operate in underwater environments [4–6]. The four part series by Shahinpoor and Kim has proven to be a seminal work, and serves as a source of information regarding a wide range of topics relating to IPMCs such as modeling, fabrication, and applications in modern technology [7–10]. More recent reviews have demonstrated the trajectory of IPMC research and development, and highlight the ongoing interest in these materials for advanced actuators and sensors [11–13].

1.2. Nondimensional multiphysics modeling framework

A new multiphysics modeling framework for IPMC materials has recently been developed which utilizes a finite-strain formulation, accounting for hyperelastic material models and the porous structure of the polymer membrane [14]. The governing equations were derived from a scalar thermodynamic free energy potential formed as an additive decomposition of the skeletal free energy in terms of mechanical, ionic, solvent, polarization, and volumetric components. This work also presented a comprehensive nondimensionalization of the kinematically linearized governing equations, with a complete list of dimensionless Π-groups, see table 1, which define the degrees of freedom parametrizing the transduction behavior of the IPMC.

The nondimensional form of the governing equations, written in terms of the Π-groups, are obtained directly from [14] but presented here with a brief explanation for completeness. The electrochemical behavior of the IPMC is governed by the interaction of mobile ionic species inside the polymer and the electrical connections to the external surface electrodes. Inside the polymer, the electric potential obeys Poisson's equation:

$$-\hat{\nabla}\cdot\hat{\nabla}\hat{\phi} = \frac{\Pi_{15}\Pi_9}{\Pi_8}\left(\hat{c}_+ - 1\right) \tag{1.1}$$

whereas the electric potential in the electrode domain is calculated via differential Ohm's law. In this model, the electrodes are treated as purely superficial, i.e. having zero thickness, and relation between the surface current density in these domains and the displacement current inside the membrane form the following equation which holds along the surface electrodes

$$\hat{\nabla}_S\cdot\hat{\nabla}_S\hat{\phi} = \Pi_{17}\frac{\partial}{\partial\hat{t}}\left(\hat{\nabla}\hat{\phi}\cdot\overline{n}\right). \tag{1.2}$$

wherein $\hat{\nabla}_S$ is the (dimensionless) surface gradient operator, which is defined along surfaces in the domain topology (i.e. 2D surfaces for 3D domains and 1D boundaries for 2D domains) and is computed using what's called the surface projection tensor, $\underline{\underline{\mathbb{P}}}$. The surface projection tensor is a rank-2 tensor that extracts the components of an entity which lie along the surface with outward normal $\overline{n}$. The surface gradient, surface divergence, and the surface projection tensor are defined below [14–17]

$$\nabla_S(\square) = \nabla(\square)\,\underline{\underline{\mathbb{P}}}. \tag{1.3a}$$

$$\nabla_S\cdot(\square) = \mathrm{tr}\left(\nabla(\square)\,\underline{\underline{\mathbb{P}}}\right) \tag{1.3b}$$

$$\underline{\underline{\mathbb{P}}} = \underline{\underline{I}} - \underline{n}\otimes\underline{n} \tag{1.3c}$$

Table 1. Dimensionless groups describing IPMC actuator and sensor transduction.

Dimensionless group	Physical description	Shorthand name
$\Pi_1 = \frac{c_{w,0}}{c_{+,0}}$	Initial ratio of solvent to mobile ionic species	Concentration number
$\Pi_2 = \frac{\mathcal{D}_w}{\mathcal{D}_+}$	Ratio of diffusivity in solvent and mobile ionic species	Diffusion number
$\Pi_3 = \nu_+ c_{+,0}$	Initial volume fraction of ionic species	Ionic fraction
$\Pi_4 = \frac{\nu_w}{\nu_+}$	Relative volume of solvent to ionic species on molar basis	Solvent size
$\Pi_5 = \frac{k_f \mathcal{C}_E}{\mathcal{D}_+}$	Hydraulic advection versus diffusive transport	Hydraulic number (Olsen-Kim 1)
$\Pi_6 = \frac{l}{h}$	Aspect ratio of IPMC as length vs thickness	Aspect ratio
$\Pi_7 = \frac{\phi_{a,c}}{\phi_{\text{th}}} = \frac{\mathcal{F}\phi_{a,c}}{RT}$	Driving input for IPMC actuator/electromigration	Driving potential
$\Pi_8 = \frac{\epsilon\left(\frac{\phi_{\text{th}}}{h}\right)^2}{\mathcal{C}_E}$	Stress contribution due to electrostatic/Maxwell tensor	Maxwell Number (Olsen-Kim 2)
$\Pi_9 = \frac{RTc_{+,0}}{\mathcal{C}_E}$	Stress contribution due to osmotic pressure	Osmotic Number (Olsen-Kim 3)
$\Pi_{10} = \mathcal{C}_\nu$	Poisson ratio of linear elastic material	Poisson ratio
$\Pi_{11} = n_{dw}$	Number of solvent molecules transported via mobile ions	Solvent drag coefficient
$\Pi_{12} = \frac{\tau_\rho}{\tau_\mathcal{D}} = \frac{\mathcal{D}_+}{h^2}\sqrt{\frac{\rho h l}{\mathcal{C}_E}}$	Mechanical versus diffusive timescales	Mechanical dynamics
$\Pi_{13} = \tau_\mathcal{D}\omega = \frac{h^2\omega}{\mathcal{D}_+}$	Driving frequency for dynamic loading	Driving frequency
$\Pi_{14} = \frac{c_{-,0}}{c_{+,0}}$	Ratio of fixed to mobile ion concentration at electroneutrality	Electroneutrality number
$\Pi_{15} = z_+$	Charge number for mobile ionic species	Mobile charge number
$\Pi_{16} = \frac{z_-}{z_+}$	Ratio of charge numbers for fixed and mobile ionic species	Charge ratio
$\Pi_{17} = \frac{\tau_{r_e}}{\tau_\mathcal{D}} = \frac{\epsilon r_e^S \mathcal{D}_+}{h}$	Resistive versus diffusive timescales	Resistive dynamics (Olsen-Kim 4)
$\Pi_{18} = \frac{u_{a,c}}{l}$	Driving input for IPMC sensor/advective migration	Driving displacement
$\Pi_{19} = \frac{h}{\lambda_d} = h\mathcal{F}\sqrt{\frac{z_+^2 c_{+,0}}{\epsilon RT}}$	Ratio of ionomer thickness to Debye screening length	Reciprocal double layer

[a] Recreated from [14].

wherein $\text{tr}(\square)$ is the trace operator. Inside the membrane, the cation and solvent species experience coupled diffusion, electromigration, convection, and saturation driven transport phenomena

$$\frac{\partial \hat{c}_+}{\partial \hat{t}} = \hat{\nabla}\cdot\left(\hat{\nabla}\hat{c}_+ + \Pi_{15}\hat{c}_+\hat{\nabla}\hat{\phi} + \frac{\Pi_3}{\Pi_9}\hat{c}_+\hat{\nabla}\hat{\mathcal{P}} + \Pi_1\Pi_2\hat{n}'_{d+}\left(\hat{\nabla}\hat{c}_w + \frac{\Pi_3\Pi_4}{\Pi_9}\hat{c}_w\hat{\nabla}\hat{\mathcal{P}}\right) + \Pi_5\hat{c}_+\hat{\nabla}\left(\hat{\wp} - \hat{\mathcal{P}}\right)\right). \tag{1.4a}$$

$$\frac{\partial \hat{c}_w}{\partial \hat{t}} = \hat{\nabla}\cdot\left(\frac{\hat{n}'_{dw}}{\Pi_1}\left(\hat{\nabla}\hat{c}_+ + \Pi_{15}\hat{c}_+\hat{\nabla}\hat{\phi} + \frac{\Pi_3}{\Pi_9}\hat{c}_+\hat{\nabla}\hat{\mathcal{P}}\right) + \Pi_2\left(\hat{\nabla}\hat{c}_w + \frac{\Pi_3\Pi_4}{\Pi_9}\hat{c}_w\hat{\nabla}\hat{\mathcal{P}}\right) + \Pi_5\hat{c}_w\hat{\nabla}\left(\hat{\wp} - \hat{\mathcal{P}}\right)\right) \tag{1.4b}$$

$$\hat{n}'_{d+} = \begin{cases} \dfrac{\Pi_{11}}{\Pi_1\Pi_2} & \dfrac{\hat{c}_+}{\hat{c}_w} > \dfrac{\Pi_1\Pi_2}{\Pi_{11}^2} \\ \dfrac{\Pi_{11}}{\Pi_1\Pi_2}\dfrac{\hat{c}_+}{\hat{c}_w} & \dfrac{\hat{c}_+}{\hat{c}_w} \leqslant \dfrac{\Pi_1\Pi_2}{\Pi_{11}^2} \end{cases},$$

$$\hat{n}'_{dw} = \begin{cases} \Pi_{11}\dfrac{\hat{c}_w}{\hat{c}_+} & \dfrac{\hat{c}_+}{\hat{c}_w} > \dfrac{\Pi_1\Pi_2}{\Pi_{11}^2} \\ \Pi_{11} & \dfrac{\hat{c}_+}{\hat{c}_w} \leqslant \dfrac{\Pi_1\Pi_2}{\Pi_{11}^2} \end{cases}. \tag{1.5}$$

In the derivation of the governing equations, the porosity of the membrane evolves according to a similar transport relation but is constrained via the saturation condition to account for the total volume for an ideal mixture of ions and solvent species. This constraint is achieved via the Lagrange multiplier, $\hat{\mathcal{P}}$, which is named the Lagrange pressure. The Lagrange pressure works in conjunction with the conjugate pressure, $\hat{\wp}$, which is work conjugate to the volume expansion of the solid membrane. The difference in these two pressures, $\hat{\wp} - \hat{\mathcal{P}}$, found in the transport relations is the pore pressure of the saturating fluid. Under the influence of the Lagrange pressure, the porosity is constrained to the follow:

$$\hat{\lambda} = \Pi_3 \left(\hat{c}_+ + \Pi_1 \Pi_4 \hat{c}_w \right). \tag{1.6}$$

Conservation of linear momentum leads to a statement of mechanical equilibrium between the inertial effects of the combined solid/fluid porous medium, external loading, and the internal stresses within the IPMC. In this model, the fluid inertia effects are ignored along with any external body loads, leading to the following equilibrium equation:

$$\left(1 - \hat{\lambda}_0\right) \Pi_{12}^2 \frac{\partial^2}{\partial \hat{t}^2} = \hat{\nabla} \cdot \underline{\underline{\hat{\sigma}}}^T. \tag{1.7}$$

The Cauchy stress tensor, $\underline{\underline{\hat{\sigma}}}$, is additively decomposed into mechanical, osmotic, and polarization contributions along with the conjugate pressure to obtain the effective stress in the membrane. These components and the decomposition are defined below

$$= \underline{\underline{\hat{\sigma}}}_{\text{mech}} + \underline{\underline{\hat{\sigma}}}_{\text{osmotic}} + {}_{\text{pol}} - \hat{\wp} \underline{\underline{I}} \tag{1.8a}$$

$$\underline{\underline{\hat{\sigma}}}_{\text{mech}} = \frac{1}{1 + \Pi_{10}} \left(\frac{\Pi_{10}}{1 - 2\Pi_{10}} \text{tr} \left(\underline{\underline{\hat{\varepsilon}}} \right) \underline{\underline{I}} + \underline{\underline{\hat{\varepsilon}}} \right) \tag{1.8b}$$

$$\underline{\underline{\hat{\sigma}}}_{\text{osmotic}} = \Pi_9 \left[(1 - \hat{c}_+) + \Pi_1 (1 - \hat{c}_w) \right] \underline{\underline{I}} \tag{1.8c}$$

$$\underline{\underline{\hat{\sigma}}}_{\text{pol}} = \Pi_8 \left(\underline{\hat{d}} \otimes \underline{\hat{d}} - \frac{1}{2} \left(\underline{\hat{d}} \cdot \underline{\hat{d}} \right) \underline{\underline{I}} \right) \tag{1.8d}$$

$$\hat{\wp} = -\frac{1}{3} \frac{1}{(1 - 2\Pi_{10})} \frac{1}{1 - \hat{\lambda}} \left(\frac{\hat{\lambda}_0 - \hat{\lambda}}{1 - \hat{\lambda}_0} + \Pi_6 \hat{\nabla} \cdot \underline{\hat{u}} \right) \tag{1.8e}$$

wherein the osmotic component accounts for osmotic pressure due to both ionic and solvent species redistribution, and the polarization component gives rise to the Maxwell stress. In the Maxwell stress, the dimensionless electric displacement is related to the dimensionless electric potential as $\underline{\hat{d}} = \hat{\nabla} \hat{\phi}$. The mechanical component amounts to an isotropic, linear elastic material model with the infinitesimal strain tensor suitability nondimensionalized as:

$$\underline{\underline{\hat{\varepsilon}}} = \frac{1}{2} \Pi_6 \left(\hat{\nabla} \underline{\hat{u}} + \left(\hat{\nabla} \underline{\hat{u}} \right)^T \right). \tag{1.9}$$

The strain tensor is itself a nondimensional quantity, but in the process of nondimensionalization of the governing equations there is a characteristic scaling of the strain tensor, evidenced by the occurrence of the aspect ratio (Π_6) in the above definition. In the cited work, it was demonstrated that when formulating the Π-groups on the basis of an actuator or sensor formulation there are slight differences in the resulting set of physically independent Π-groups. In particular, the driving potential (Π_7) characterizes the magnitude of the input voltage for an IPMC actuator, whereas the driving displacement (Π_{18}) takes its place for an IPMC sensor. More interesting is that in the actuator derivation the Maxwell number (Π_8) arises whereas in the sensor derivation this dimensionless number is not found and, in its place, the reciprocal double layer (Π_{19}) is obtained [14]. A short analysis demonstrates that these two dimensionless numbers are not physically independent and hence cannot occur in the same set of Π-groups for characterizing the transduction phenomena. The relationship between the reciprocal double layer, charge number, osmotic number, and Maxwell number is given below, the utility of which will be demonstrated later

$$\Pi_{19}^2 = \frac{\Pi_{15}^2 \Pi_9}{\Pi_8}. \tag{1.10}$$

The electromechanical response of an IPMC can manifest in the displacement of the material as well as produce an actuating force. Thus far, the equations provided can be combined with simple displacement boundary conditions to simulate the actuator displacement. To simulate the force response of the IPMC some further considerations are necessary. When constrained, the IPMC produces an actuating force. In measuring this force value, the IPMC is typically placed against a force transducer such that the sensor blocks the IPMC deformation, and hence the resulting load is commonly referred to as the IPMC blocking force. Here the model is extended to allow for simulating the blocking force of the IPMC. Considering a 2D model of a cantilever IPMC our approach to constraining the IPMC deformation is the application of a surface traction to the free end. This traction vector will be used to constrain the transverse deformation of the thin cantilever strip, which is assumed to be aligned lengthwise with the x-axis and the through-the-thickness direction with the y-axis. The surface traction applied at the tip of the IPMC can be expressed as:

$$\underline{t} = \begin{bmatrix} 0 \\ -t_{\mathcal{R}} \end{bmatrix}. \tag{1.11}$$

The value of this applied traction is zero in the x-component to leave the axial deformation unconstrained. The y-component of the applied traction takes a value of $-t_{\mathcal{R}}$, the negative of the traction load generated by the force transducer. The value for this traction is calculated as a Lagrange multiplier imposed to constrain the average transverse tip deflection to be zero, i.e.

$$\langle v \rangle = 0, \ \text{on} \partial \Omega_{\text{tip}}. \tag{1.12}$$

Ultimately the total reaction force offers a better metric by which to compare the multiphysics model to potential experiments. The total reaction force, $\mathcal{R}$, is found by integrating the surface traction across the domain boundary which it is applied, hence

$$\mathcal{R} = \int_{\partial \Omega_{\text{tip}}} t_{\mathcal{R}} dS. \tag{1.13}$$

The surface traction may be nondimensionalized using characteristic stress, and using equation (1.13), a nondimensional reaction force may be computed as:

$$\Pi_{\mathcal{R}} := \hat{\mathcal{R}} = \frac{\mathcal{R}}{F_c} = \frac{\sigma_c w h}{F_c} \int_{\partial \Omega_{\text{tip}}} \hat{t}_{\mathcal{R}} d\hat{S}. \tag{1.14}$$

If we assume the IPMC to have a rectangular cross-section of width w and thickness h, and define our characteristic force as $F_c = \sigma_c wh$ one arrives at the following relation between the nondimensional blocking force and the applied surface traction calculated as a Lagrange multiplier

$$\Pi_{\mathcal{R}} = \int_{\partial\Omega_{\text{tip}}} \hat{t}_{\mathcal{R}} d\hat{\ell} = \hat{t}_{\mathcal{R}}. \tag{1.15}$$

The Lagrange multiplier may be easily implemented in the weak formulation for a finite element model and provides a simple approach to simulating the blocking force of the IPMC.

Like in electromechanical transduction, the mechanoelectrical response of IPMC materials exhibits two distinct modes depending on the external electrical connection of the electrodes, short-circuit current and open-circuit voltage. The short-circuit sensing current can be established on as the difference of the surface currents entering the superficial electrodes, or as the difference in displacement current integrated along the electrode-polymer interface, all while both electrodes are short-circuited to ground. In this work equation (1.16*a*) is used to compute the dimensionless short-circuit current

$$\Pi_I := \hat{I}_{\text{sc}} = -\frac{1}{\Pi_{17}} \left(\left(\hat{\nabla}_S \hat{\phi} \cdot \underline{n}_C \right)_- - \left(\hat{\nabla}_S \hat{\phi} \cdot \underline{n}_C \right)_+ \right). \tag{1.16a}$$

$$\hat{I}_{\text{sc}} = -\left(\int_{\hat{L}_-} \frac{\partial}{\partial \hat{t}} \left(\hat{\nabla} \hat{\phi} \cdot \underline{n} \right) d\hat{\ell} - \int_{\hat{L}_+} \frac{\partial}{\partial \hat{t}} \left(\hat{\nabla} \hat{\phi} \cdot \underline{n} \right) d\hat{\ell} \right). \tag{1.16b}$$

The open-circuit voltage can be established as a floating potential for one of the electrode contacts while the other remains grounded. In this model the open-circuit voltage is computed as the difference between upper $(+)$ and lower $(-)$ clamp voltages, and the lower electrode domain is grounded, hence:

$$\Pi_\phi := \hat{\phi}_{\text{oc}} = \hat{\phi}_- - \hat{\phi}_+ = -\hat{\phi}_+. \tag{1.17}$$

The computation of the open-circuit voltage may be accomplished by the means of a Lagrange multiplier used to constrain the net current flowing through the IPMC to be zero, i.e. the upper electrode clamp voltage takes on the value of negative the Lagrange multiplier which constrains the short-circuit current to be zero at all times.

2. Nondimensional parametric study of IPMC transduction behavior

The primary objective of this study is to quantify the influence of each Π-group on the IPMC transduction behavior. To this end, we individually vary each Π-group while holding the remaining groups fixed at a fixed value. Using the material properties given in [14] we can establish a fixed value for each Π-group around which the parametric study will be performed.

Table 2. Fixed value for IPMC Π-groups.

Π-group	Value
Π_1	12.278
Π_2	70
Π_3	1.6754×10^{-2}
Π_4	1.3892
Π_5	1.8
Π_6	160
Π_7	9.9068
Π_8	1.019×10^{-7}
Π_9	5.2419×10^{-3}
Π_{10}	0.45
Π_{11}	4
Π_{12}	9.2376×10^{-10}
Π_{13}	3125
Π_{15}	1
Π_{17}	7.2×10^{-12}
Π_{18}	0.03
Π_{19}	226.82

Table 3. Sets of Π-group values for parametric study.

Π-group	Sweep set
Π_1	8, 10, 12, 15, 20
Π_2	2, 10, 25, 50, 100
Π_3	5.0×10^{-3}, 7.5×10^{-3}, 1.0×10^{-2}, 1.5×10^{-2}
Π_4	1.0×10^{-1}, 5.0×10^{-1}, 1, 1.5, 2.0
Π_5	1.0×10^{-1}, 2.5×10^{-1}, 5.0×10^{-1}, 1, 2
Π_6	25, 50, 150, 200
Π_7	-10, -1, 1, 5, 10, 20, 40
Π_8	1.0×10^{-8}, 1.0×10^{-7}, 5.0×10^{-7}, 1.0×10^{-6}, 2.0×10^{-6}
Π_9	1.0×10^{-3}, 2.5×10^{-3}, 7.5×10^{-3}, 1.0×10^{-2}, 2.5×10^{-2}
Π_{10}	0.35, 0.4, 0.45, 0.49
Π_{11}	1, 2, 3, 4, 5, 6
Π_{12}	1×10^{-11}, 1×10^{-10}, 1×10^{-9}
Π_{13}	2^{10}, 2^{11}, 2^{12}, 2^{13}, 2^{14}
Π_{15}	-3, -2, -1, 1, 2, 3
Π_{17}	1.0×10^{-12}, 1.0×10^{-10}, 5.0×10^{-10}, 1.0×10^{-9}
Π_{18}	5×10^{-3}, 1×10^{-2}, 5×10^{-2}, 1×10^{-1}, 2.5×10^{-1}
Π_{19}	100, 250, 500, 1000, 2500, 5000

These fixed values are provided in table 2, while the set of values over which the parameters will be swept are given in table 3. The transduction behavior for the actuator and sensor models are characterized for both static and dynamic inputs then metrics to quantify the results further are formulated and analyzed.

2.1. *Influence of dimensionless groups in IPMC actuators*

2.1.1. Tip displacement. Beginning with the IPMC actuator model, we sweep each Π-group across its respective range and observe the behavior the transverse tip displacement, Π_Δ, in time. We first examine the static response of the IPMC to a

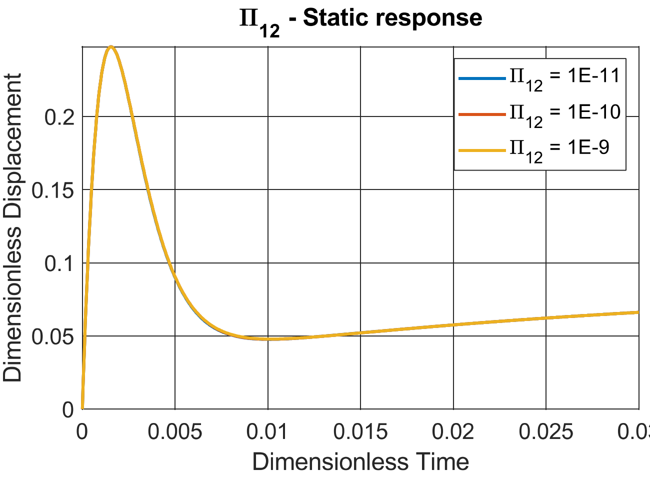

Figure 1. Static response of IPMC actuator with varying Mechanical Dynamics.
In the above plot the three time-traces are indistinguishable, indicating that the IPMC actuator response is essentially invariant to changes in the Mechanical Dynamics. This amounts to the mechanical balance behaving quasi-statically.

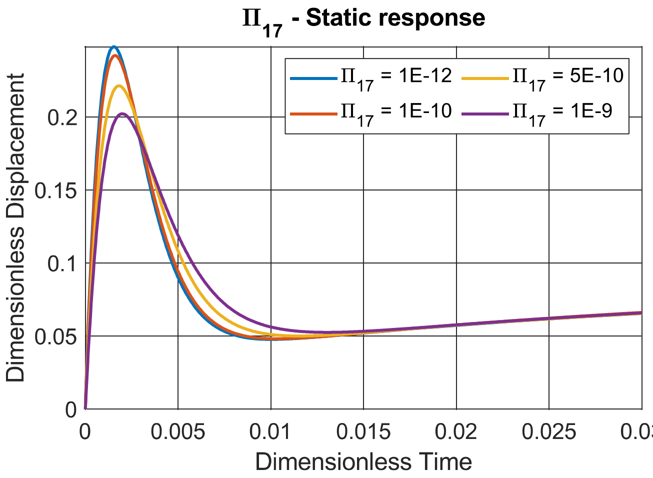

Figure 2. Static response of IPMC actuator with varying resistive dynamics.
Unlike with varying Mechanical Dynamics, the Resistive Dynamics show a marked effect on the static response of the IPMC. This effect though is only on the initial transience, and does not affect the steady-state deformation.

step input of voltage. The dimensionless external potential is applied to the upper electrode clamp. Here only the results of those parametric sweeps that were found to be most interesting are presented and discussed, but the results the remaining parametric studies are provided in the supplemental material (available online at stacks.iop.org/SMS/31/025014/mmedia).

To begin, we find that the Mechanical Dynamics (Π_{12}) have virtually no effect on the behavior of the IPMC in the range investigated, shown in figure 1. For a typical IPMC, the Mechanical Dynamics takes on a small magnitude and only arises in the governing equations as the leading coefficient of the acceleration in equation (1.7). This situation renders the mechanics quasi-static, where the displacement field responds near instantaneously to the stresses induced inside the membrane. The existence of this small parameter multiplying the time derivative would allow for a perturbative expansion of the equilibrium equation to obtain the quasi-static solution at the zeroth order, and a first order correction that includes the relevant dynamics. This approach would find use in analyzing the modal response of IPMCs or possibly in a damped structural model but is not investigated in this study.

We also find that the Resistive Dynamics (Π_{17}, OK4) have a marked effect on the initial peak displacement and transient behavior of the IPMC, but the steady-state response of the IPMC settles to the same value (see figure 2). This is intuitively understood as the surface resistance affecting the time it takes for the electric potential along the length of the IPMC to stabilize. Since the IPMC electrodes are open-circuited at the terminal end we find the induced displacement currents settle to zero as time proceeds regardless of the surface resistivity, and hence the steady-state is invariant with respect to the Resistive Dynamics. This also highlights the naming convention for this Π-group, as the resistivity of the electrode affects the displacement currents, which are by nature transient and are important for the dynamic behavior but play no role in the steady-state response for a static input. A similar behavior is observed in figure 3 with respect to the Solvent

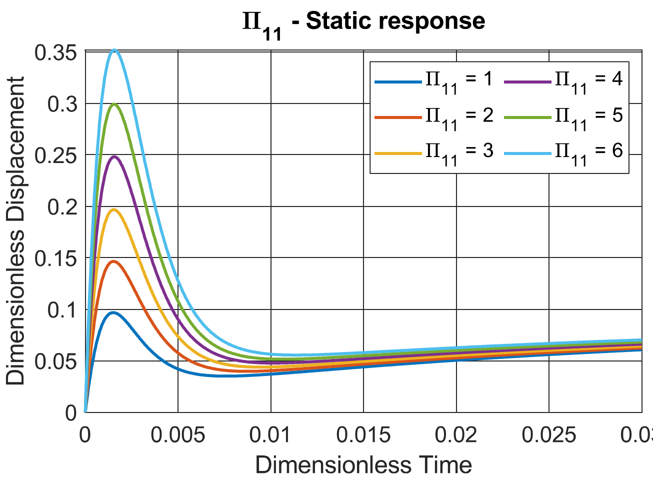

Figure 3. Static response of IPMC actuator with varying solvent drag coefficient.
Variations in the Solvent Drag Coefficient show a similar characteristics to those in the Resistive Dynamics, wherein the initial transience is influenced greatly while the steady-state response is marginally affected.

Drag Coefficient (Π_{11}), whereby there is a marked affect in the initial transience that fades as the response stabilizes. This is attributed to the Solvent Drag Coefficient describing the ion and solvent transport due to transport of one species relative to another, and hence these effects are dynamic in nature.

Two dimensionless groups that are of interest in the displacement analysis are the Maxwell Number (Π_8, OK2) and the Osmotic Number (Π_9, OK3). The Osmotic Number and Maxwell Number are connected to the osmotic pressure and Maxwell stress, shown in equations (1.8*c*) and (1.8*d*) respectively. It is widely accepted that the forward deformation mechanism is due to the redistribution of mobile ions and so connected to the osmotic pressure, while more recent studies have connected the back-relaxation phenomena to be cause, in part, by the asymmetric electric field and the Maxwell stress

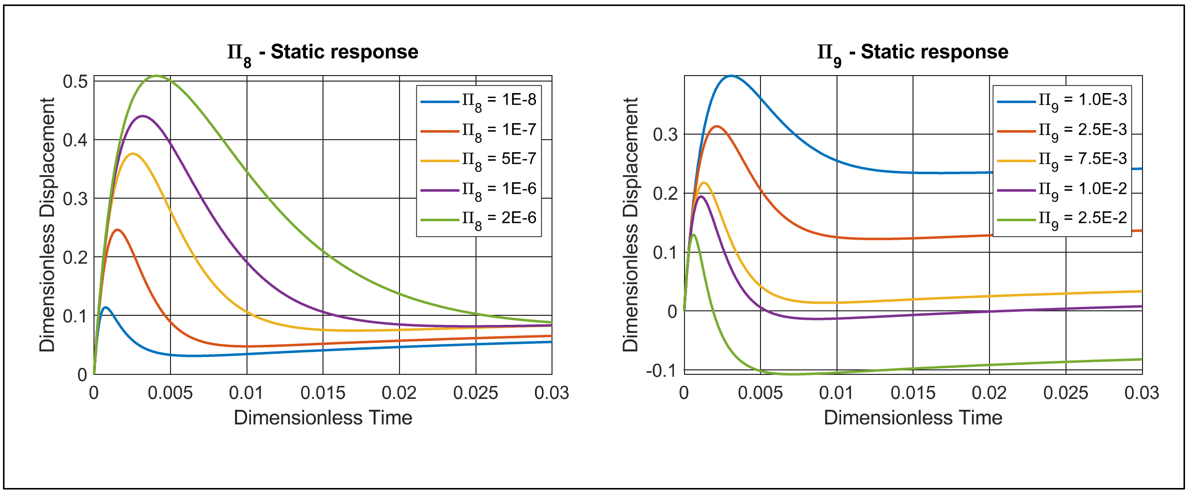

Figure 4. Influence of Maxwell number and osmotic number on static displacement.
The Maxwell Number and Osmotic Number, related to the Maxwell stress and osmotic pressure respectively, show an interesting, counterintuitive behavior discussed in detail within the text.

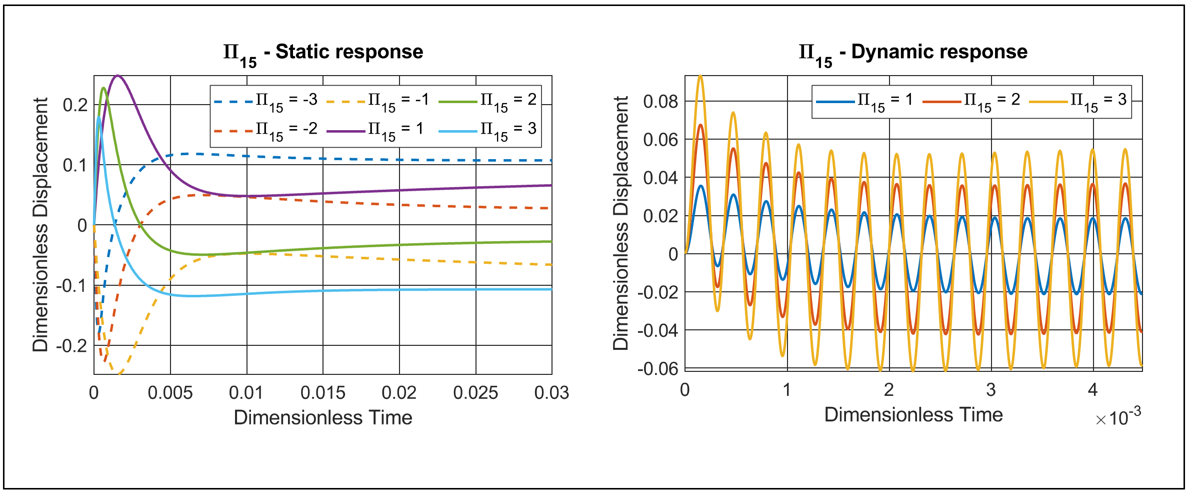

Figure 5. Influence of mobile charge number on static and dynamic displacement response.
The Mobile Charge Number has an inverse effect on the static and dynamic displacement. For static inputs the peak displacement decreases with increased Mobile Charge Number, whereas the dynamic amplitude increases.

[7, 9, 18–21]. Hence, these two dimensionless groups deserve special attention when characterizing the IPMC transduction behavior. The static response of the IPMC for the parametric studies of these parameters are presented together in figure 4, but the discussion of the behavior is reserved until after the dynamic response has been presented.

To study the response of the IPMC to dynamic input voltages, a sinusoidal potential was applied to the upper electrode. Much of the behavior found in the static response of the IPMC is again displayed in the dynamic response. Aside from the Driving Potential (Π_7), we find that the Ionic Fraction (Π_3), Solvent Size (Π_4), Aspect Ratio (Π_6), and Driving Frequency (Π_{13}) exhibit the strongest effect on the dynamic actuator response. Interestingly the Mobile Charge Number has an inverse effect on the dynamic response as compared with the static response (see figure 5). As the Mobile Charge Number (Π_{15}) increases in magnitude the peak static response decreases while the back-relaxation phenomenon is accentuated, while the dynamic response amplitude simply increases.

We attribute this to the higher charge number being associated with stronger electromigration and electrostatic forces, which not only increases the speed at which the ionic redistribution occurs but also amplifies the effects of back-relaxation due to the quadratic dependence of the Maxwell stress on the electric potential. In the dynamic case, we find a large amplitude due to the increased ionic redistribution and hence osmotic pressure, but the back-relaxation affects are diminished for reasons to be explained shortly. First, we have to examine the dynamic response to variations in the Maxwell Number and Osmotic Number, given in figure 6.

To facilitate the comparison of the static and dynamic behavior we construct metrics by which to quantitatively compare the transduction response of the two modes against each other. For the static input we opt to choose the initial peak response

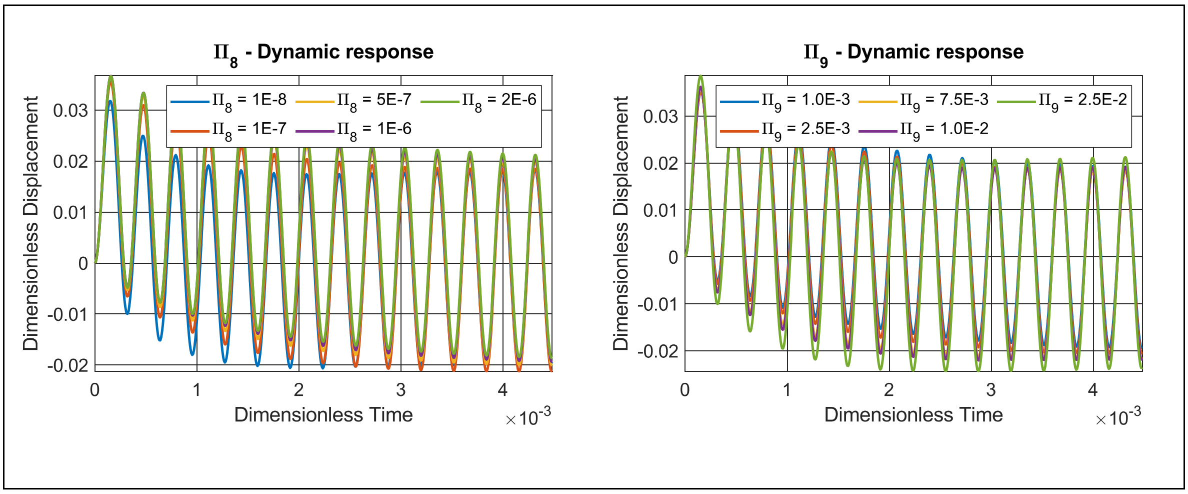

Figure 6. Influence of Maxwell number and osmotic number on dynamic displacement.
The Maxwell Number and Osmotic Number, related to the Maxwell stress and osmotic pressure respectively, show an interesting, counterintuitive behavior discussed in detail within the text.

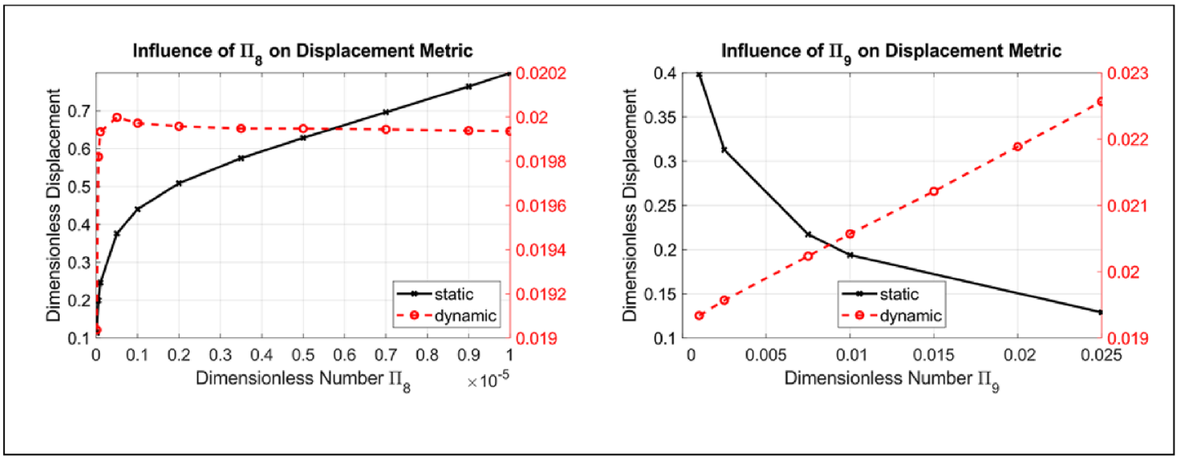

Figure 7. Maxwell number and osmotic number displacement metrics.
The displacement metrics better demonstrate the described counterintuitive behavior found in the Maxwell Number and Osmotic Number.

of the signal as our metric, whereas for the dynamic input the amplitude of the sinusoidal response is extracted via discrete Fourier transform (DFT). These metrics will be used to compare the static and dynamic response for actuator displacement, current sensing, and voltage sensing and the full results are provided in the supplemental material. Here we present the results for the Maxwell Number and Osmotic Number in the case of the actuator displacement in figure 7.

Comparing the static and dynamic metrics we see that both the Osmotic Number (Π_9) and Maxwell Number (Π_8) note the *counterintuitive effect* these dimensionless groups have on the actuator response. In the static response, we find that increasing the Osmotic Number leads to a decreased peak displacement and increased back relaxation effect, while increasing the Maxwell Number leads to a significant increase in peak displacement with a marginal effect on the back-relaxation of the steady-state. The converse is true for the dynamic response, wherein we find that with an increase in Osmotic Number there is a corresponding increase in actuator amplitude, and for an increase in Maxwell Number there is a small decrease in amplitude. This observation is counterintuitive because, as stated previously, the Osmotic Number and Maxwell Number are directly tied to the osmotic pressure and Maxwell stress, respectively, and hence one would expect that an increase in either dimensionless number would have a corresponding increase in their respective stress contribution. This interesting behavior is connected to the discussion regarding the physical independence of the Π-groups as it pertains to the actuator and sensor formulations. The initial analysis found a connection between the Reciprocal Double Layer, Mobile Charge Number, Osmotic Number, and Maxwell Number [14], which was reiterated in equation (1.10).

It is already known that in IPMC electrochemistry under a dimensionless framework the PNP system is found to be singularly perturbed in space, that is, there is a small parameter multiplying the highest order spatial derivative in the equations, and in this case it arises in the Poisson equation for electrostatics, equation (1.1), [21–23]. This leads to the

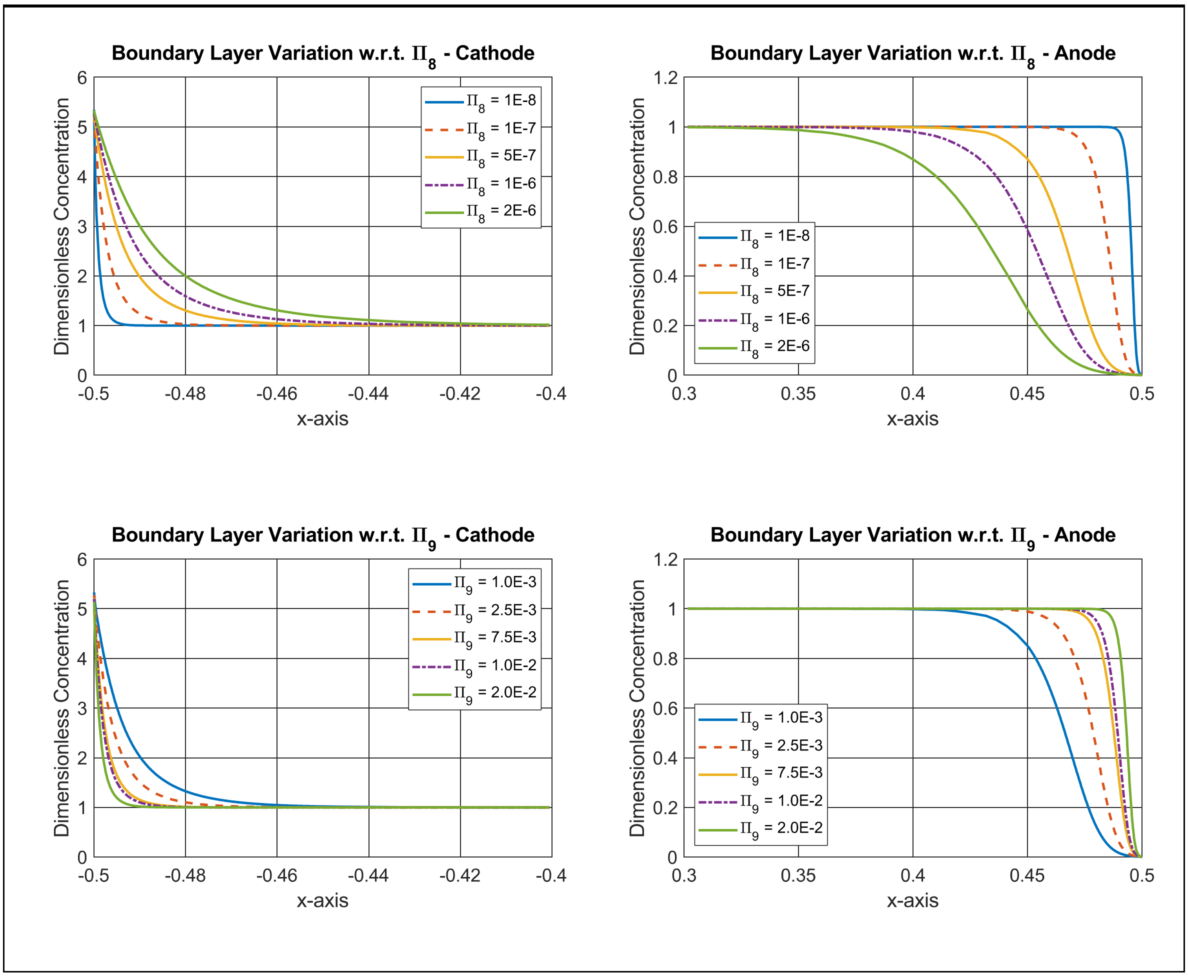

Figure 8. Concentration boundary layer with respect to osmotic and Maxwell numbers.
The above plots demonstrate the effect of increasing the Osmotic Number and Maxwell Number on the boundary layer that forms in the concentration field at the polymer-electrode interface.

formulation of boundary layers in the vicinity of the polymer-electrode interface which facilitate the application of perturbation methods in forming semi-analytic solutions to these problems [22–25]. These boundary layers are regions in which the solution varies rapidly from its value outside of the layer, in the bulk of the membrane. Of interest to us is the relation of the currently established Π-groups with this boundary layer formation near the polymer-electrode interface. Blending the dimensionless framework used here with the techniques used in literature, the perturbation expansion parameter would be taken as [14, 21–23]:

$$\delta = \frac{\sqrt{\Pi_{15}}}{\Pi_{19}} = \sqrt{\frac{\Pi_8}{\Pi_9 \Pi_{15}}}. \tag{2.1}$$

This number is small for a typical IPMC, and hence is useful in the previously mentioned asymptotic techniques. As this quantity decreases in value the boundary layers sharpen and we find an increase in the asymmetry of the electric potential. Due to the quadratic nature of the Maxwell stress, the asymmetry in electric potential gradients is key to this stress's contribution to back-relaxation phenomenon, and hence an increase in the asymmetry is linked to an increase in back-relaxation and a corresponding decrease in forward displacement of the IPMC. These effects on the boundary layer are illustrated below for the ionic concentration, electric potential, and electric field in the through-the-thickness direction in figures 8–10 respectively.

Now we can make sense of the curious behavior seen in the parametric study on the actuator displacement. For the static response, an increase in the Osmotic Number leads to a sharpening of the boundary layers and increased Maxwell stress-induced back-relaxation. Increasing the Maxwell Number *counterintuitively* diminishes the influence of the Maxwell stress by broadening the boundary layers and reducing the asymmetry in the electric potential profiles. This allows for the osmotic pressure to dominate, leading to higher peak and steady-state displacements.

Looking at the dynamic response we saw the opposite trend. This is explained by the fact that back-relaxation occurs over a longer timescale. This is true for back-relaxation due to solvent back-diffusion, as well as for the Maxwell stress induced back-relaxation. In regard to the Maxwell stress, the delay in the onset of back-relaxation may be attributed to the

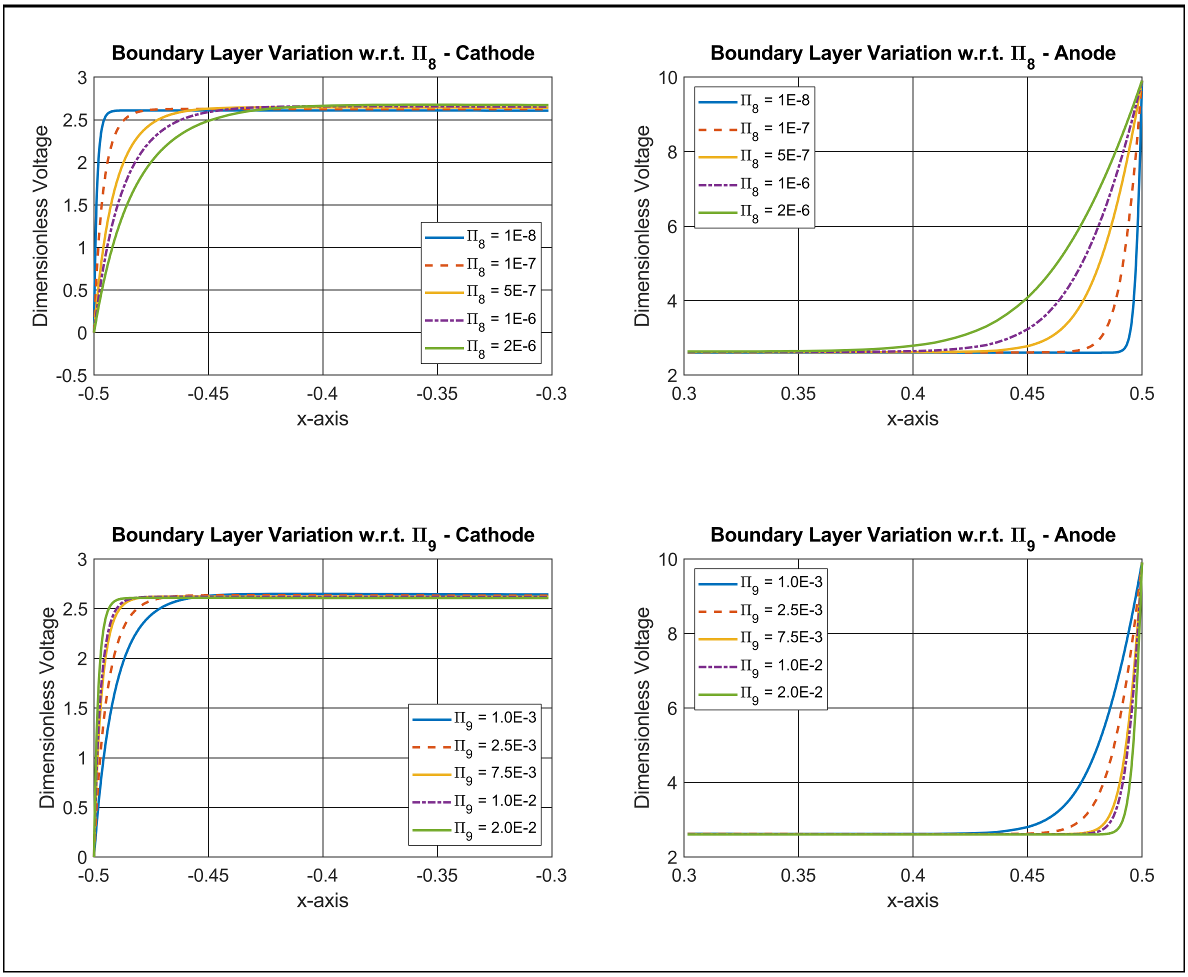

Figure 9. Electric potential boundary layer with respect to osmotic and Maxwell numbers. The above plots demonstrate the effect of increasing the Osmotic Number and Maxwell Number on the boundary layer that forms in the electric potential at the polymer-electrode interface.

time it takes for the electric potential field to stabilize and form asymmetric boundary layers. For dynamically applied voltages, the internal electric potential is constantly varying and hence the asymmetry in the boundary layers have little time to establish themselves. This leads to a diminished effect of both the Osmotic Number and Maxwell Number on the boundary layer thickness, and hence the overall electrostatic back-relaxation is of minimal influence. The end result is that under a dynamic voltage input with increasing Osmotic Number, the corresponding sharpening of the boundary layers is nullified by the electric potential being constantly varied throughout the membrane and hence the increase in osmotic pressure dominates, leading to increased displacement response. For the Maxwell Number, we see only a minimal influence on the displacement amplitude as its effect scales the magnitude and influence of the Maxwell stress, which is diminished due to the asymmetry in electric potential being not fully establishing itself because of the transient nature of the potential field. Additionally, this explanation extends to the behavior seen in the Mobile Charge Number and the differences in the static and dynamic response with respect to variations in this dimensionless group.

2.1.2. Blocking force. Turning now from the actuator displacement to the blocking force generation, the same parametric study is performed here, and the complete results are provided in the supplemental material. Without presenting all of the cases here, we note that the results of the parametric study for the actuator blocking force near identically match those of the actuator displacement, differing only in magnitude, and with the one exception of the Aspect Ratio (see figures 11 and 12, respectively, for example).

This curiosity applies to both the static and dynamic response and inspires further investigation. To probe this behavior, we look to leverage the closed form solutions for beam bending found in introductory texts on structural mechanics. In particular, under the assumptions of infinitesimal linear elasticity, uniaxial stress, and a Hooke's law stress–strain relation the tip deflection of a cantilevered beam under an applied point load at the free end has an analytical solution. Translating this solution into the current dimensionless framework, one can write the following relation between the dimensionless deflection, Π_Δ, and dimensionless applied load, $\Pi^*_{\mathcal{R}}$. The superscripted asterisk denotes the load as calculated via linear structural mechanics

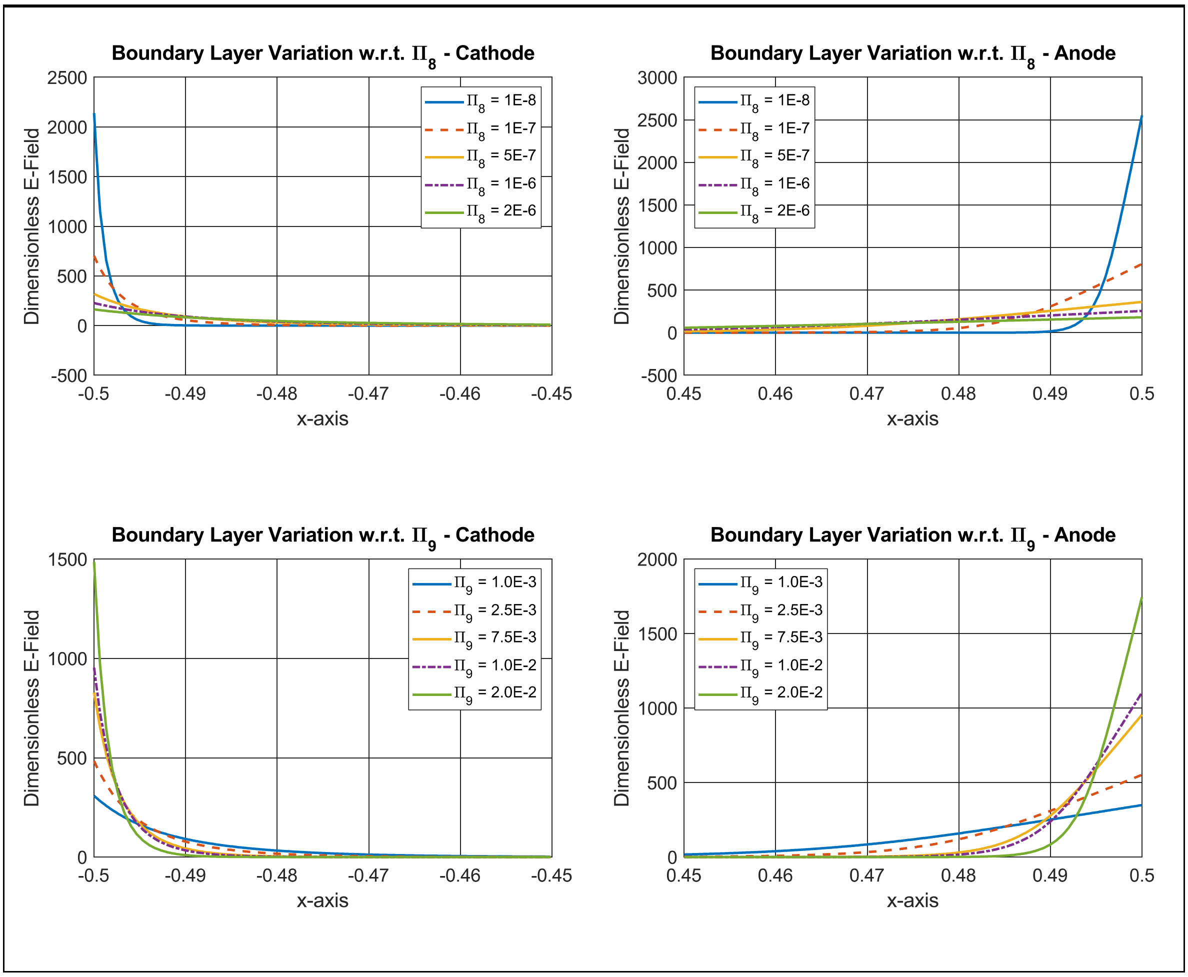

Figure 10. Electric field boundary layer with respect to osmotic and Maxwell numbers.
The above plots demonstrate the effect of increasing the Osmotic Number and Maxwell Number on the boundary layer that forms in the electric field at the polymer-electrode interface.

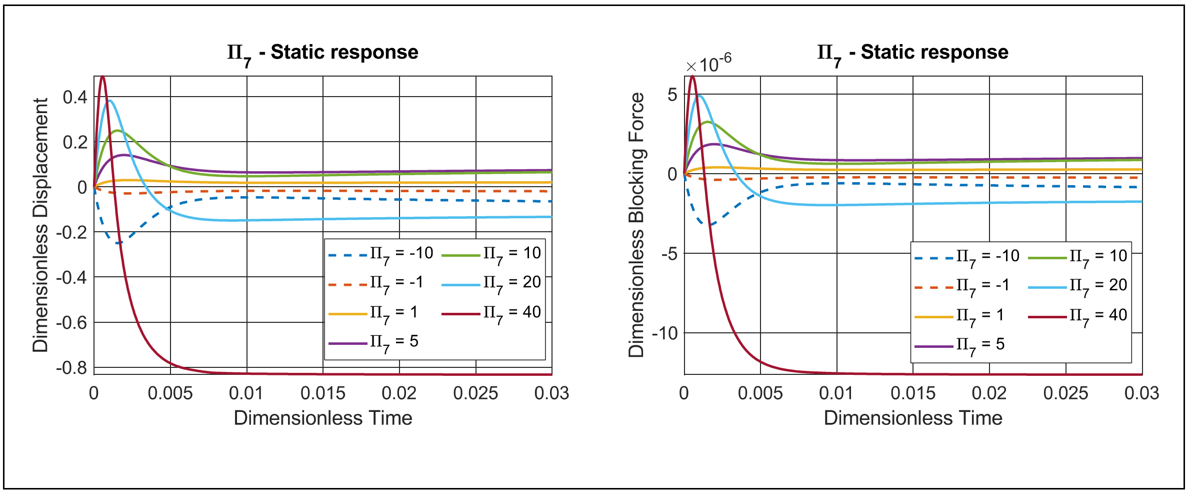

Figure 11. Influence of driving potential on static displacement and blocking force.
The driving potential, a measure of the applied voltage used as an input to the electromechanical model, has a marked effect on the static displacement response. A nearly identical behavior is found in the blocking force among almost all Π-groups.

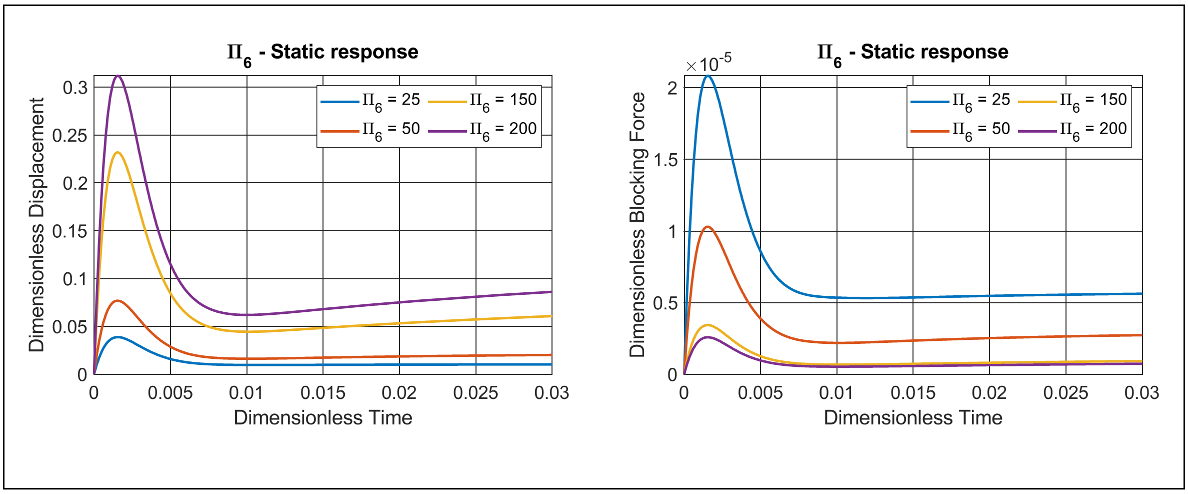

Figure 12. Influence of aspect ratio on static displacement and blocking force.
The Aspect Ratio is the sole parameter for which the actuator displacement and blocking force exhibit different responses. While in the displacement we find a roughly linear increase with increasing Aspect Ratio, the blocking force exhibits an asymptotic decrease.

$$\Pi^*_{\mathcal{R}} = \frac{\Pi_\Delta}{4\Pi_6^2}. \tag{2.2}$$

A common practice in linear structural mechanics is to invoke the principle of superposition, wherein the response of a beam to combined loading is the superposition of the beam's response to each loading separately. This would imply that we may calculate the IPMCs reaction force by first allowing the IPMC to deform, and then use the above relation to calculate the force needed to negate the resulting deformation. Here we do not presume that the internal loading of the IPMC will necessarily follow the principle of superposition, but instead look for a relation between the true dimensionless blocking force, $\Pi_{\mathcal{R}}$, calculated as a one-parameter function of the approximation from linear structural mechanics, i.e.

$$\Pi_{\mathcal{R}} = f(\Pi^*_{\mathcal{R}}). \tag{2.3}$$

Such a relation would characterize the blocking force transduction response entirely in terms of the dimensionless actuator response, forming a powerful connection between the two transduction modes that may be leveraged in experiments or design studies. The dimensionless blocking force according to equation (2.3) is calculated directly from the previously obtained actuator displacement results. Here we establish the following relations between the true and linear beam reaction force for static (2.4*a*) and dynamic (2.4*b*) inputs

$$\Pi_{\mathcal{R}} = \frac{4}{3}\Pi^*_{\mathcal{R}} = \frac{1}{3}\frac{\Pi_\Delta}{\Pi_6^2}. \tag{2.4a}$$

$$\Pi_{\mathcal{R}} = \frac{29}{21}\Pi^*_{\mathcal{R}} = \frac{29}{84}\frac{\Pi_\Delta}{\Pi_6^2}. \tag{2.4b}$$

The fitting coefficients were fit qualitatively via trial and error and then formulated into low complexity rational numbers just for the sake of demonstration. These relations offer remarkable performance in approximating the blocking force as calculated from the multiphysics model for being derived from linear structural mechanics and inspired by the principle of superposition (see figures 13 and 14).

In the plots below the reaction force as calculated in the multiphysics model with the Lagrange multiplier is rendered as the line, whereas the force calculated using (2.4*a*) or dynamic (2.4*b*) are rendered in symbols. In the static response the symbols are spaced logarithmically to capture the initial transience without overcrowding the plot, but the data itself is equally spaced in time and the logarithmic spacing is simply post-processing for visualization. In the dynamic response we use equally spaced symbols, but only the last period of the response is presented for easier visualization of the results.

The relation in equation (2.2) also explains the sole discrepancy in the match between actuator displacement and blocking force results with respect to the Aspect Ratio. This can be explained further as while the actuator tip displacement increases with increasing IPMC length, the internal stresses via osmotic pressure and the Maxwell stress generated within the membrane are roughly invariant with the length of the membrane. Hence, as the IPMC length increases so does the moment arm, and thus the force delivered at the tip of the IPMC decreases with increasing length from a moment balance perspective. Due to the similarities in the results for the actuator displacement and blocking force, and the derived relationship between the two, the static and dynamic response metrics for the blocking force are not explored.

2.2. *Influence of dimensionless groups in IPMC sensors*

2.2.1. Short-circuit current. Turning our attention to the mechanoelectrical transduction, we first consider the short-circuit current sensing in IPMC materials. Using essentially the same suite of parametric sweeps, we characterize the static then dynamic response. In place of the Applied Potential, we sweep across values for the Applied Displacement. Similarly, the Maxwell Number is replaced by the Reciprocal Double

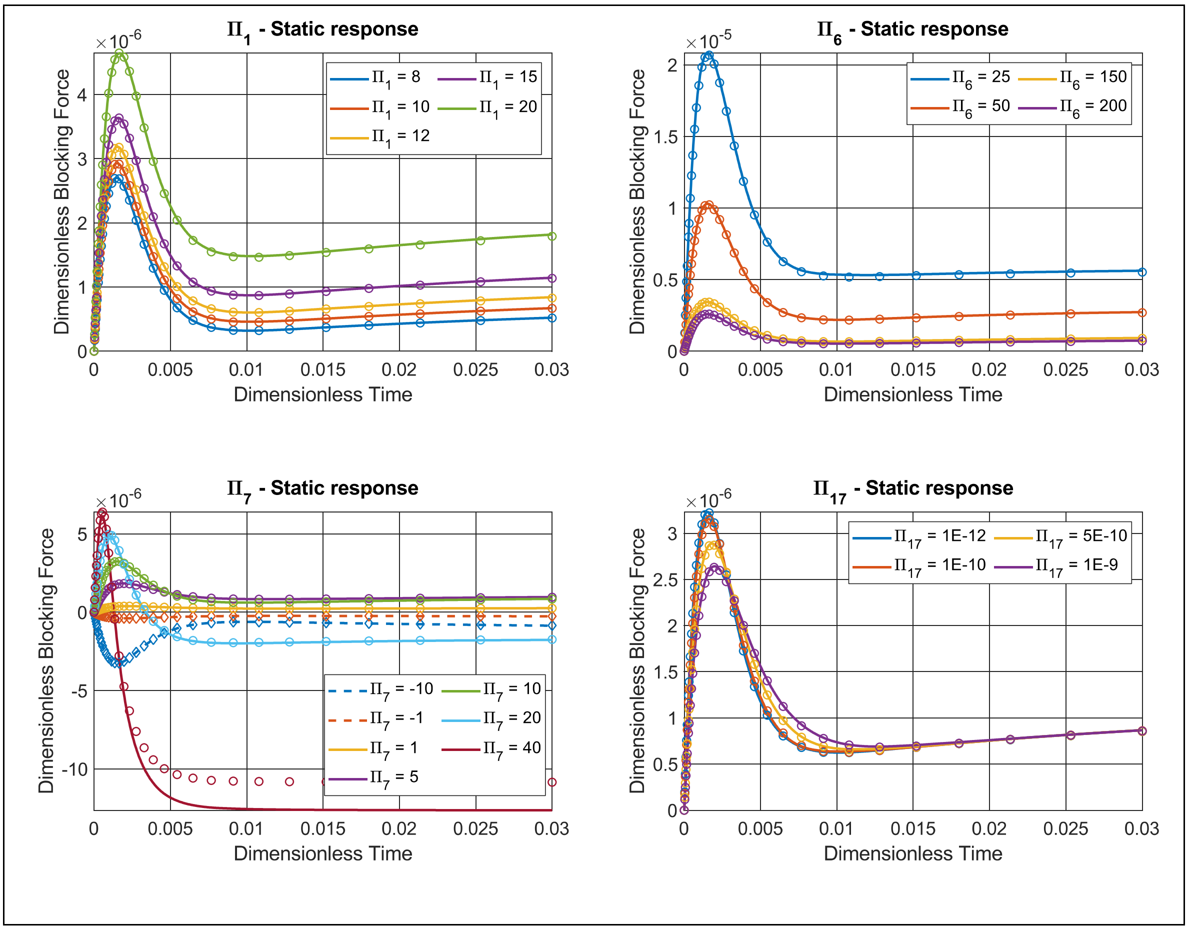

Figure 13. Comparison of multiphysics and linear beam static blocking force results.
In the above multiplot, the static blocking force as calculated via Lagrange multiplier in the multiphysics model (lines) is compared with that calculated from the displacement response via linear beam theory (symbols).

Layer. In the static response, in place of a step input we use a ramped displacement that reaches peak magnitude after 1 s in conventional (dimensional) time. This is translated back into a dimensionless framework using the characteristic time. During the analysis it was found that the static and dynamic current sensing response were quite similar, and hence the key results can be summarized by looking at only the metrics as described earlier.

We note that unlike the static actuator response, the Diffusion Number plays a minor role while the Hydraulic Number takes on significant importance for the static current response (See figure 15). Furthermore, the Osmotic Number and Solvent Drag Coefficient have negligible effects on the current (see the supplemental material). The underlying reason for these observations is the difference in driving forces behind both electromechanical and mechanoelectrical transduction mechanisms. In electromechanical transduction the driving force is the applied electric potential that induces the ionic redistribution. These electromigration affects are highly nonlinear and very strong in comparison to the diffusive and hydraulic effects. In contrast, mechanoelectrical transduction is driven by deformation induced pressure gradients inside the membrane causing advective redistribution of the mobile ions and solvent. The level of redistribution is significantly less than in electromigration, and hence the induced osmotic pressure and electric field are weaker. Furthermore, the diffusive effects associated with coupled solvent-ion transport are reduced due to the advective transport acting to move both solvent and ionic species together, and hence we expect the Diffusion Number to be less important as it characterizes a relative transport effect between the two species. Hence, we would reasonably expect that the Hydraulic Number to play a dominant role in mechanoelectrical transduction as this Π-group characterizes the strength of the bulk advection of the solvent and ionic species, the latter of which is the generation of the sensing current.

Additionally, both the Resistive Dynamics (figure 16) and Reciprocal Double Layer (figure 17) have a strong influence on the current response. The sensing current is seen to decrease sub-linearly with the Resistive Dynamics. Making allowances for some variation due to resistive effects, a given level of deformation should lead to approximately the same level of ionic redistribution due to advective effects in of the bulk fluid moving through the porous structure. The sublinear features noted in the current sensing metrics can then be seen to reflect macroscopic Ohms law behavior, where for a given voltage an increase in resistance leads to a decrease in current with a linear relationship. As for the Reciprocal Double Layer, we see that increasing this value, and hence decreasing the scale of the

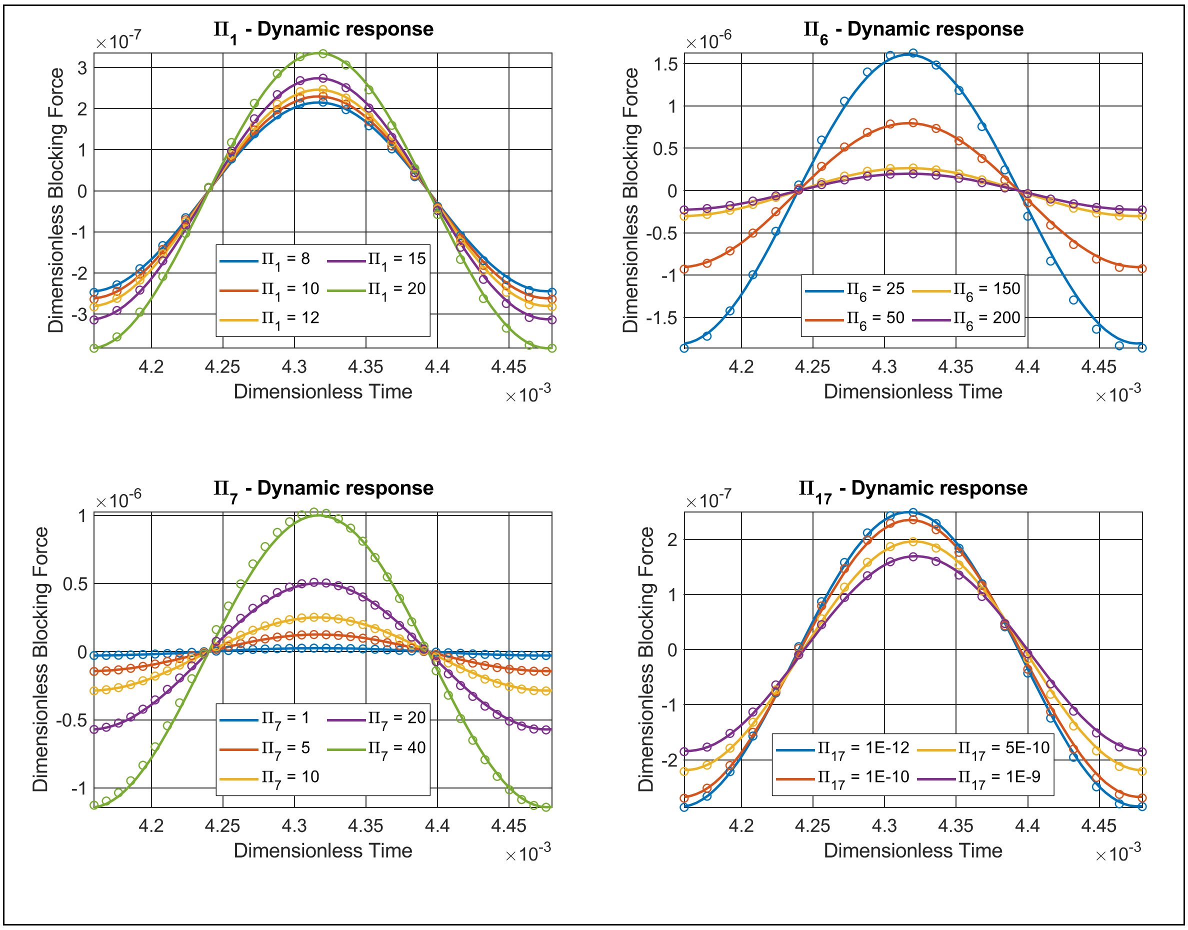

Figure 14. Comparison of multiphysics and linear beam dynamic blocking force results.
In the above multiplot, the dynamic blocking force as calculated via Lagrange multiplier in the multiphysics model (lines) is compared with that calculated from the displacement response via linear beam theory (symbols).

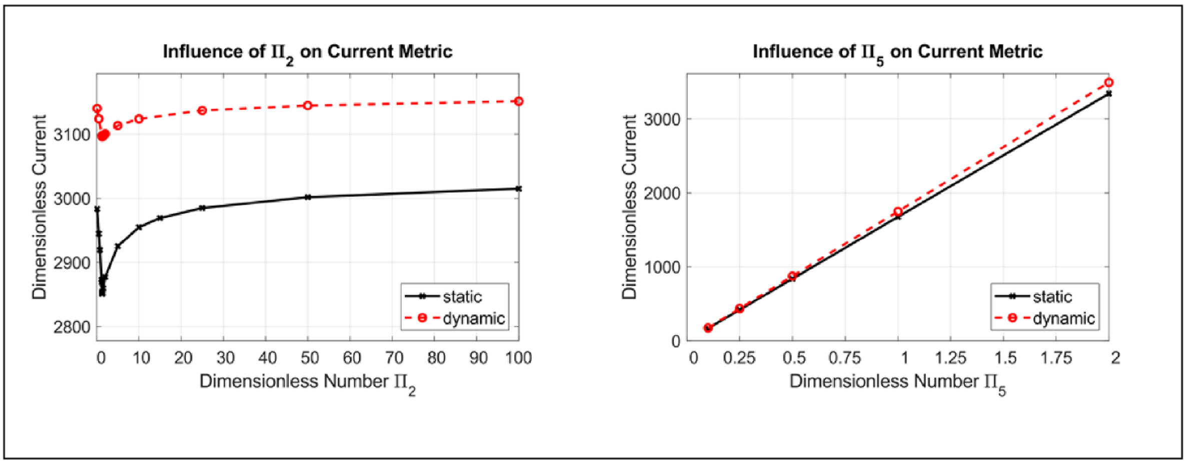

Figure 15. Influence of diffusion number and hydraulic number on IPMC current sensor metrics.
The above demonstrates a fundamental shift in the underlying physics driving the electromechanical and mechanoelectrical transduction. In the case of electromechanical transduction the diffusion and coupled solvent and ion transport played an important role, the bulk advection of the species was minor. Here we show the reverse is true for mechanoelectrical transduction, wherein bulk advection in the pore fluid is one of the major underlying phenomena driving the IPMC response.

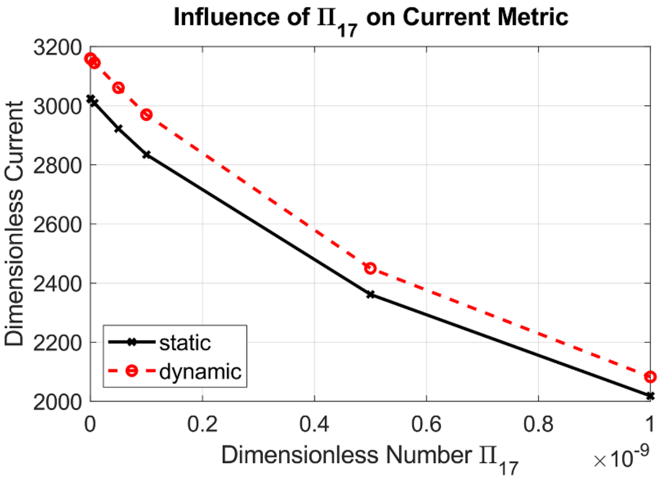

Figure 16. Influence of the resistive dynamics on IPMC short-circuit current metrics.
Our analysis finds that the short-circuit current response decreases sublinearly with increasing Resistive Dynamics, indicating that the effects of resistive electrodes degrade the performance of the IPMC as a current sensor.

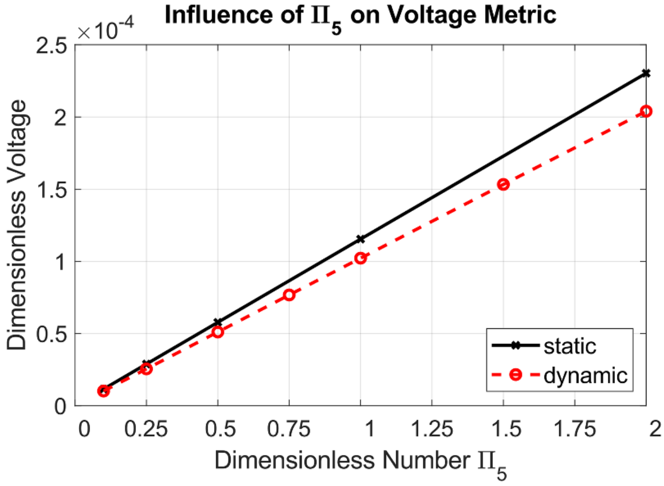

Figure 18. Influence of the hydraulic number on IPMC open-circuit voltage metrics.
As was the case in current sensing, the Hydraulic Number plays a major role in the voltage sensing response. Here we find a roughly linear relationship between the voltage metric and the Hydraulic Number.

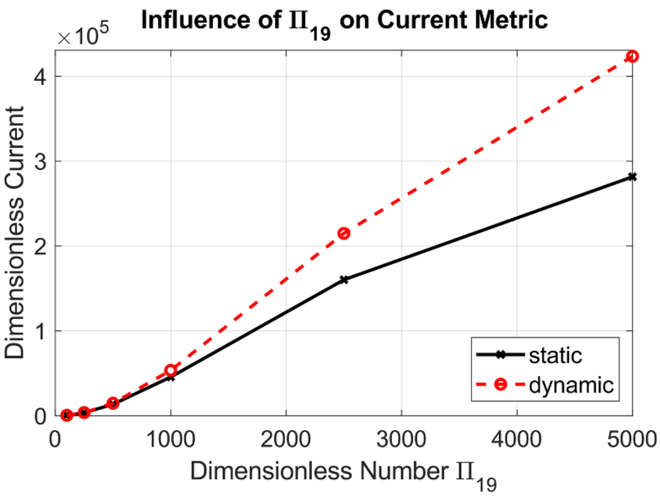

Figure 17. Influence of the reciprocal double layer on IPMC short-circuit current metrics.
The Reciprocal Double Layer has a curious influence on the sensing current, wherein we find an increase initially, but the effects decrease as the double layer narrows.

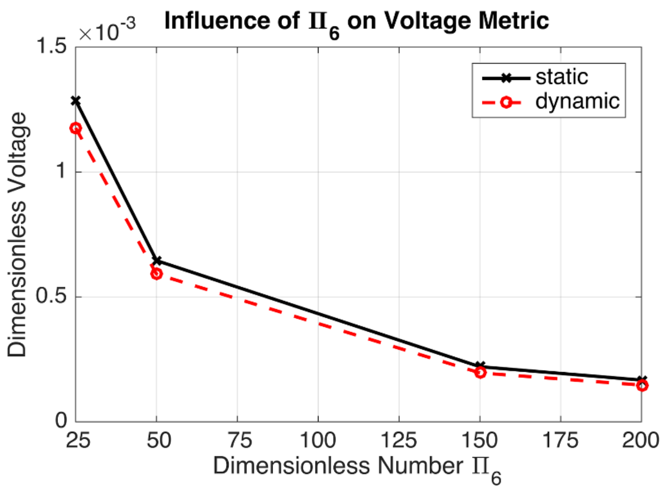

Figure 19. Influence of the aspect ratio on IPMC open-circuit voltage metrics.
As was the case in current sensing, the Hydraulic Number plays a major role in the voltage sensing response. Here we find a roughly linear relationship between the voltage metric and the Hydraulic Number.

double layer region, we obtain higher sensing currents. This is explained in connection to the thinner double layers charging more quickly and inducing larger charge in the electrodes which drive the sensing current. As a final note, we very little phase change or amplitude variation with Driving Frequency, and the current response displays a linearly increasing phase lag with increasing Reciprocal Double Layer, with a total shift of $\sim 17°$ across the range of parameter values tested.

2.2.2. Open-circuit voltage. Finally, we look at the open-circuit voltage response of the IPMC. Again, we repeat this same analysis for the open-circuit voltage response under static and dynamic loads and follow up with an analysis on the voltage metrics under these conditions across a set of Π-values that capture the interesting aspects of this transduction mode. As with the short-circuit current the static and dynamic response demonstrate nearly identical behavior when using their respective metrics to compare the two input types and hence can use these results to explore the transduction behavior.

Again, the osmotic and diffusive effects play a secondary role in the open-circuit voltage response while the bulk pore fluid has a significant impact via the Hydraulic Number (figure 18). The same arguments for explaining this phenomenon in the current sensor model apply here to the voltage response. Interestingly, we find that the Aspect Ratio (figure 19) plays a substantial role in the voltage response, whereas it had virtually no role in the current response.

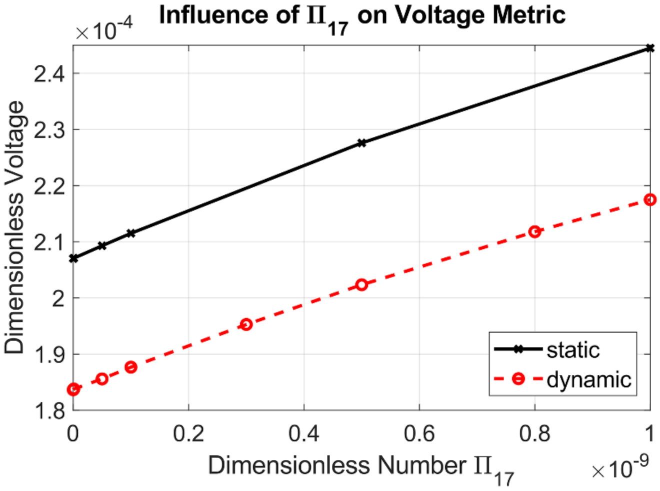

Figure 20. Influence of resistive dynamics on IPMC open-circuit voltage metrics.
The open-circuit voltage metrics show a sub-linear increase in the response with increasing Resistive Dynamics. This is described within the manuscript; for a level of deformation the ionic current generated remains roughly the same, and hence with increasing resistance one finds an increase in voltage.

We also find a somewhat reduced influence from the Resistive Dynamics (figure 20) as compared to the current sensing model, and a starkly more complex behavior when it relates to the Reciprocal Double Layer for both the static and dynamic inputs (figure 21) with what a damping of the initial voltage peak for the static response, and a significant phase shift and amplitude variation in the dynamic response.

Of particular interest to us is the relationship to the Reciprocal Double Layer, where a strong degree of phase shift is observed as this Π-group lowers in value. As we saw in the actuator model with Resistive Dynamics, the Reciprocal Double Layer introduces an additional timescale associated with the double layer formation

$$\tau_{\lambda_d} = \frac{\tau_{\mathcal{D}}}{\Pi_{19}}. \tag{2.5}$$

We see that there is a reciprocal relationship between this timescale and the Π-group (hence our naming convention). Intuitively, an increase in the Reciprocal Double Layer indicates thinner ionic double layers, which are capable of charging faster and hence feature faster dynamic behavior. As this value decreases, the double layer charging slows, and we see additional dynamic effects in the open-circuit voltage response associated with this timescale. When looking at the influence of the Reciprocal Double Layer on the dynamic voltage phase we see this reciprocal dependence on the Π-group, and hence a direct dependence on the double layer timescale τ_{λ_d}, shown in figure 22.

Furthermore, we find that the dynamic voltage response shows a significantly higher degree of decay (figure 23) and phase shift (figure 24) with increasing Driving Frequency as compared to the dynamic current response. We calculate the phase by finding the complex angle between the peaks in input and output signals obtained from the DFT analysis. This result makes the phase relation more explicit, wherein we can see that the dynamic voltage response transitions from lagging to leading the displacement input after $\Pi_{19} \approx 1000$. The leading behavior of IPMC voltage sensing has been demonstrated previously in experimental settings [26]. There is a phase shift induced with changing Resistive Dynamics, but again these are negligible and amount to $\sim 3°$ across the range of the parametric sweep.

3. Constructing regression models using dimensionless groups

With the significant insights obtained in the proceeding analysis, we now look to constructing functional relationships that capture some of these results in the form of regression models. To this end, we have restricted our analysis only to that of dynamic actuator displacement and dynamic open-circuit voltage sensing. The goal is to obtain regression models that can be used to predict the behavior of the full multiphysics model within the vicinity of our operating point (i.e. the parameters given in table 2). Formulating a regression model for the actuator/sensor metrics is a tall order as the problem exists in a high-dimensional solution space (one dimension for each Π-group). Hence, we first look to establish a means of reducing the complexity of the regression problem into a larger number of more manageable sub-problems.

3.1. Decomposition of the transduction response

To begin, note the influence of each individual Π-group on the metric in question could be easily regressed in a one-dimensional solution space and each metric plot presented in the supplemental material was constructed by varying a single Π-group while the remaining Π-groups are held fixed. The fixed values for the Π-group effectively describe an origin of the high-dimensional solution space in which we are attempting to formulate a regression model. The metric plots can then be imagined as slices of an unknown function along the coordinate axes of this high-dimensional space which correspond to each independent Π-group.

In order to formulate a regression model for the desired transduction response we leverage the physical independence of the Π-groups and propose that the IPMC response may be approximated by a multiplicative decomposition of the variations with respect to each Π-group individually. To elaborate, given some unknown function f that describes the transduction response with respect to the set, $\{\Pi\}$, of relevant Π-groups. By holding all Π-groups fixed except Π_i we find the response can be modeled as a one-dimensional function, $f_i(\Pi_i)$, i.e. the behavior captured in our parametric studies

$$f(\{\Pi\})\,|_{\{\Pi\}\setminus\Pi_i} = f_i(\Pi_i)\,. \tag{3.1}$$

Our proposal is that the complete response f may be *approximated* by a multiplicative decomposition of these single Π-group functions

$$f(\{\Pi\}) \approx f_1(\Pi_1) f_2(\Pi_2) \cdots f_n(\Pi_n)\,. \tag{3.2}$$

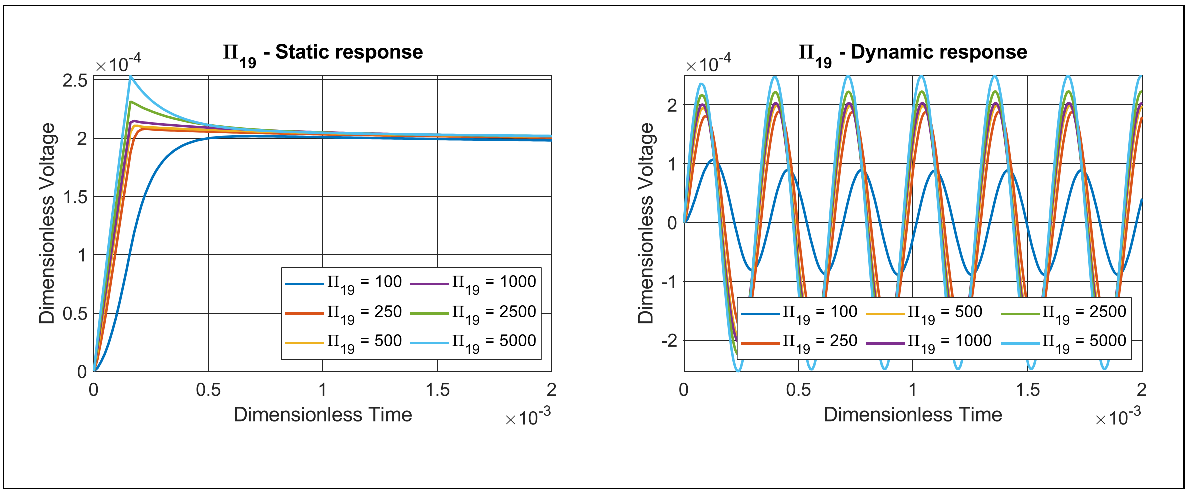

Figure 21. Influence of the reciprocal double layer on static and dynamic voltage response.
The Reciprocal Double Layer is found to have a stronger influence on the open-circuit voltage as compared to the short-circuit current response, exhibiting amplitude and phase variations in the static and dynamic cases.

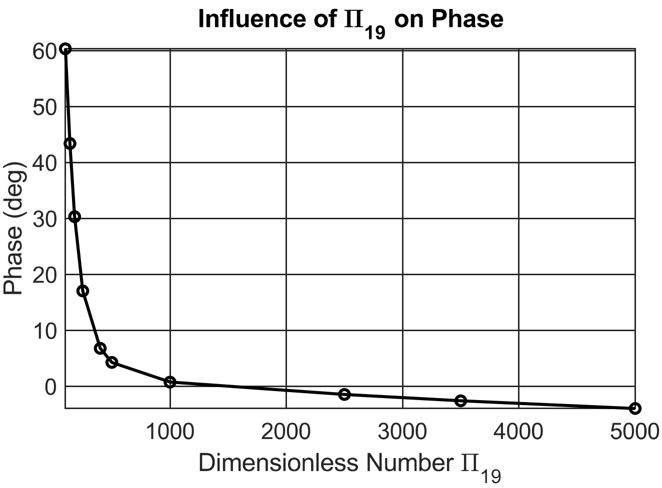

Figure 22. Reciprocal double layer induced phase shift in dynamic voltage response.
Discussed in the text, the variation of the Reciprocal Double Layer induces considerable phase change in the dynamic voltage response due to double layer charging effects operating on a timescale related to this dimensionless group.

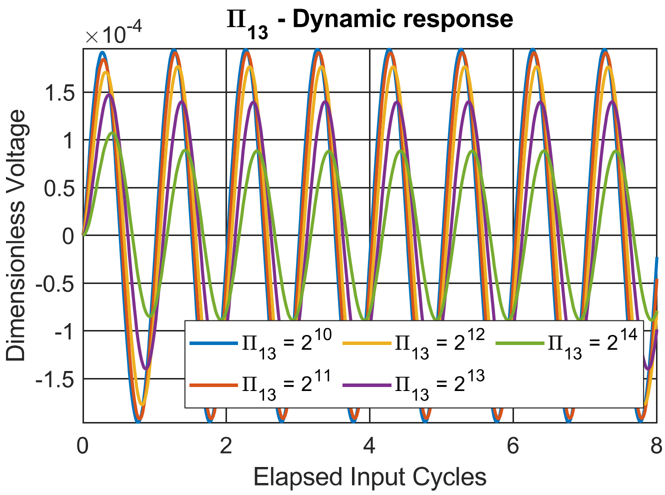

Figure 23. Influence of driving frequency on dynamic open-circuit voltage.
The open-circuit voltage exhibits an amplitude decrease with increasing frequency, typical of dynamically actuated IPMCs.

This methodology is taken as a means for simplifying the high-dimensional regression problem at hand. By embarking on this approach, we are able to model each Π-group's individual influence on the respective transduction metric, which is a simple one-dimensional regression problem. In the coming analysis, we define presumptive functional forms which are capable of capturing the behavior of each Π-group.

One further layer of simplification is a pruning of the set of Π-groups into a smaller subset of parameters which are found to have the most influence on the transduction response in question. For example, in the previous analysis we found that Π_5 and Π_{12} had nearly no effect on the dynamic displacement response, and Π_8 had only a small influence. Hence, these dimensionless numbers are removed from the set of Π-groups and thus allow for a smaller parameter space to be used.

3.2. Regression model for the dynamic actuator displacement

Here we establish the presumptive functional forms, provided in table 4, which will be used to regress the effect of each Π-group on the dynamic actuator displacement. These functions are obtained by first looking for low order polynomials that may suitably regress the data within the range of interest. If a reasonable low order polynomial cannot be fit to the data, we expand the function class to rational polynomials which offer more control over the asymptotic behavior of the function. In some instances, a rational polynomial of low order could not reasonably fit the data and so more 'exotic' function combinations were tested. These included looking at the decaying or rising behavior of the response and trying to characterize this in terms of fractional powers, exponentials, logarithms, and hyperbolic functions. Additionally, the use

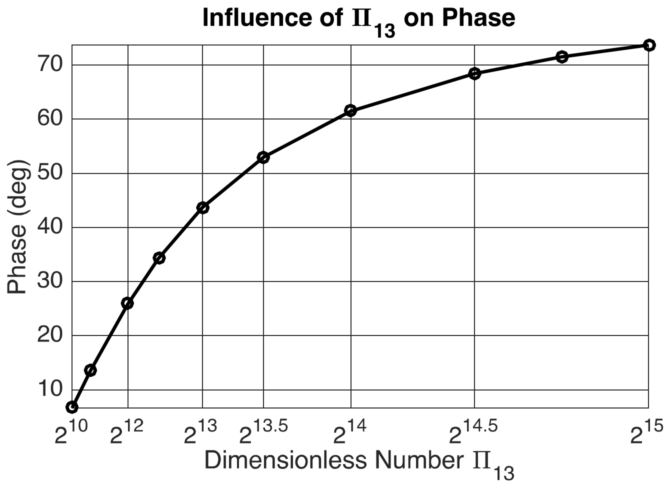

Figure 24. Driving frequency induced phase shift in dynamic voltage response.
Discussed in the text, the variation of the Reciprocal Double Layer induces considerable phase change in the dynamic voltage response due to double layer charging effects operating on a timescale related to this dimensionless group.

of symbolic regression with the GPTips toolbox was conducted on some metric plots to gain additional function combinations to explore [27]. In the end, the final function form was decided manually, using all of the previous approaches along with engineering judgment for the problem at hand. To regress each of these functions we use the *'nlinfit'* function in MATLab for nonlinear fitting. We use a termination tolerance on the estimated coefficients of 10^{-6}, a tolerance on the residual sum of squares of 10^{-7}, and bisquare robust fitting is implemented. With this approach, we obtain the regression provided in the supplemental material. In each of the one-dimensional models the regression coefficient with the highest subscript is used to normalize the function with respect to multiplication which is used when assembling the model according to a multiplicative decomposition. The regression coefficients, after normalization, are be used as initial guesses for a nonlinear fitting routine in MATLab.

For the dynamic actuator, we obtain the multiplicative model shown in equation (3.3). Notice that by normalizing the individual components we have reduced the total number of regression coefficients in this multiplicative model. To be specific, for n individual one-dimensional models, we reduce the total number of regression coefficients by $n-1$ using the multiplicative decomposition

$$\begin{aligned}\Pi_\Delta = {} & \beta_0 \Pi_6 \left|\Pi_7\right| \left(1+\beta_2\Pi_1+\beta_1\Pi_1^2\right) \\ & \times \left(1+\beta_8\Pi_2 \frac{\beta_5-\beta_6\sqrt{\Pi_2+\beta_7}-\beta_8\Pi_2-1}{1+\exp\left(-\beta_3\left(\Pi_2-\beta_4\right)\right)}\right) \\ & \times \left(1+\beta_9\Pi_3^2+\beta_{10}\Pi_3\right)\left(1+\beta_{11}\Pi_4^2+\beta_{12}\Pi_4\right) \\ & \times \left(1+\beta_{13}\Pi_9\right)\frac{\beta_{14}\Pi_{10}^2+\beta_{15}\Pi_{10}+1}{1-2\Pi_{10}} \\ & \times \left(1+\beta_{16}\Pi_{11}\right)\left(\frac{\beta_{17}}{\log\left(1+\beta_{18}\Pi_{13}\right)+\beta_{19}}+1\right) \\ & \times \left(1+\beta_{20}\tanh\left(\beta_{21}\left|\Pi_{15}\right|+\beta_{22}\right)\right) \\ & \times \left(\frac{\beta_{23}}{\sqrt{1+\beta_{24}\Pi_{17}}}+1\right). \end{aligned} \tag{3.3}$$

To visualize how well this model predicts the transduction response of the dynamic actuator, we concatenate all of the data points used in the parametric sweeps already presented. This data is sorted for easier visualization and plotted against the length of this sorted dataset. This condenses the high-dimensional data into a more easily digestible two-dimensional representation.

Demonstrated in figure 25 we find the multiplicatively decomposed model demonstrates a high degree of accuracy in predicting the transduction response and is an effective means for reducing the complexity of the high-dimensional regression. Again, the regression coefficients some error metrics for this result are provided in the supplemental material. To quantify the fit, we calculate the coefficient of determination, r^2, and the adjusted-r^2, r^2_{adj}, as below:

$$r^2 = 1 - \frac{\sum\left(y_i - y_i^*\right)^2}{\sum\left(y_i - \langle y\rangle\right)^2} \tag{3.4a}$$

$$r^2_{\text{adj}} = 1 - \frac{n-1}{n-p-1}\frac{\sum\left(y_i - y_i^*\right)^2}{\sum\left(y_i - \langle y\rangle\right)^2} \tag{3.4b}$$

wherein y_i are the data points being fit, y_i^* are the model predictions, $\langle y\rangle$ is the mean value of the data set, n is the number of data points in the set y_i, and p the degrees of freedom of the model (i.e. the number of regression coefficients). The adjusted-r^2 metric modifies the traditional coefficient of determination to address the tendency for additional model parameters to increase the r^2 value by merely reproducing the original data without providing an improved summary or interpolation of the data. For this model we find these values as $r^2 = 0.99904$ and $r^2_{\text{adj}} = 0.99571$. The two r^2 measures are provided for each of the one-dimensional models in the supplemental material.

To extract further insights into the multiplicative regression model we look to linearize the model about fixed values described by the values in table 2. To this end, we require the gradient of the regression model, and hence the first partial

Table 4. Actuator regression models for individual Π-groups.

Dimensionless group	Description of function form	Regression function
Π_1	Quadratic	$\beta_1\Pi_1^2+\beta_2\Pi_1+\beta_3$
Π_2	Linear-to-Root w/Logistic Transition	$\beta_6\Pi_2+\beta_7+\dfrac{\beta_3-\beta_4\sqrt{\Pi_2+\beta_5}-\beta_6\Pi_2-\beta_7}{1+\exp\left(-\beta_1\left(\Pi_2-\beta_2\right)\right)}$
Π_3	Quadratic	$\beta_1\Pi_3^2+\beta_2\Pi_3+\beta_3$
Π_4	Quadratic	$\beta_1\Pi_4^2+\beta_2\Pi_4+\beta_3$
Π_6	Linear	$\beta_1\Pi_6$
Π_7	Linear w/Sym.	$\beta_1\left\lvert\Pi_7\right\rvert$
Π_9	Linear	$\beta_1\Pi_9+\beta_2$
Π_{10}	Quadratic w/Pole	$\left(\beta_1\Pi_{10}^2+\beta_2\Pi_{10}+\beta_3\right)/\left(1/2-\Pi_{10}\right)$
Π_{11}	Linear	$\beta_1\Pi_{11}+\beta_2$
Π_{13}	Decaying Log	$\beta_1/\left(\log\left(\beta_2\Pi_{13}+1\right)+\beta_3\right)+\beta_4$
Π_{15}	Hyperbolic Tangent w/ Sym.	$\beta_1\tanh\left(\beta_2\left\lvert\Pi_{15}\right\rvert+\beta_3\right)+\beta_4$
Π_{17}	Decaying Root	$\beta_1/\sqrt{1+\beta_2\Pi_{17}}+\beta_3$

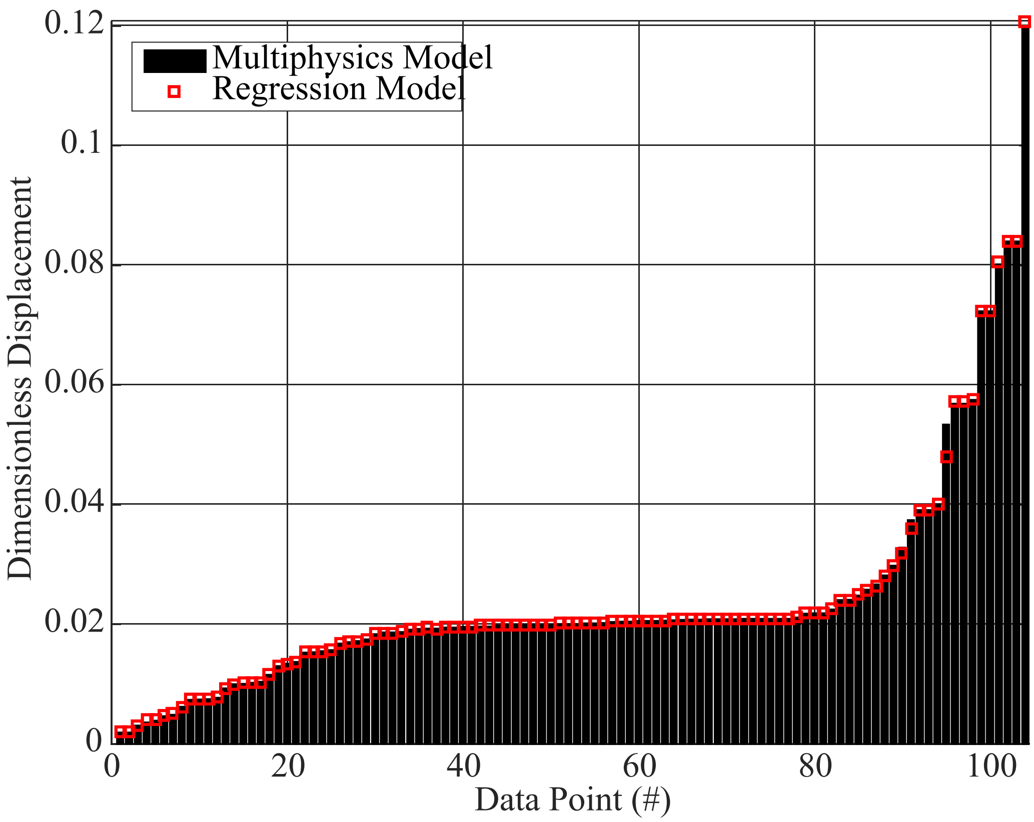

Figure 25. Bar graph of multiplicative dynamic actuator model performance.
The individual regression models are combined multiplicatively to obtain a single model for the dynamic actuator response. The above graph demonstrates the capability of this subproblem to multiplicative decomposition approach for high-dimensional regression modeling.

derivative with respect to each of the independent Π-groups. The complexity of such an expression for our current regression model defeats the purpose of simplifying the model with a linearization, and so we calculate the necessary gradient components using automatic differentiation (AD) [28]. In particular, we use an operator overloading AD approach as described in [29], where the code developed by that author is used as a basis for the *'valder'* (value-derivative) class. By declaring each Π-group as a valder object with an appropriate gradient we may simply compute the displacement metric at the fixed values and automatically obtain all necessary first partial derivatives to construct the gradient and hence a linearization of the regression model. The partial derivatives for the displacement model are provided in table 5. Using an extension of the Taylor series for multivariant functions, we can form the linear approximation as:

Table 5. First partial derivatives for multiplicative dynamic actuator model.

Partial derivative	Value	Partial derivative	Value
$\frac{\partial \Pi_\Delta}{\partial \Pi_1}$	6.9983×10^{-4}	$\frac{\partial \Pi_\Delta}{\partial \Pi_2}$	-9.4341×10^{-6}
$\frac{\partial \Pi_\Delta}{\partial \Pi_3}$	1.6728×10^{0}	$\frac{\partial \Pi_\Delta}{\partial \Pi_4}$	1.7299×10^{-2}
$\frac{\partial \Pi_\Delta}{\partial \Pi_6}$	1.2461×10^{-4}	$\frac{\partial \Pi_\Delta}{\partial \Pi_7}$	2.0125×10^{-3}
$\frac{\partial \Pi_\Delta}{\partial \Pi_9}$	1.3348×10^{-1}	$\frac{\partial \Pi_\Delta}{\partial \Pi_{10}}$	-7.9748×10^{-3}
$\frac{\partial \Pi_\Delta}{\partial \Pi_{11}}$	4.1416×10^{-3}	$\frac{\partial \Pi_\Delta}{\partial \Pi_{13}}$	-6.1524×10^{-6}
$\frac{\partial \Pi_\Delta}{\partial \Pi_{15}}$	1.9224×10^{-2}	$\frac{\partial \Pi_\Delta}{\partial \Pi_{17}}$	-1.3635×10^{7}

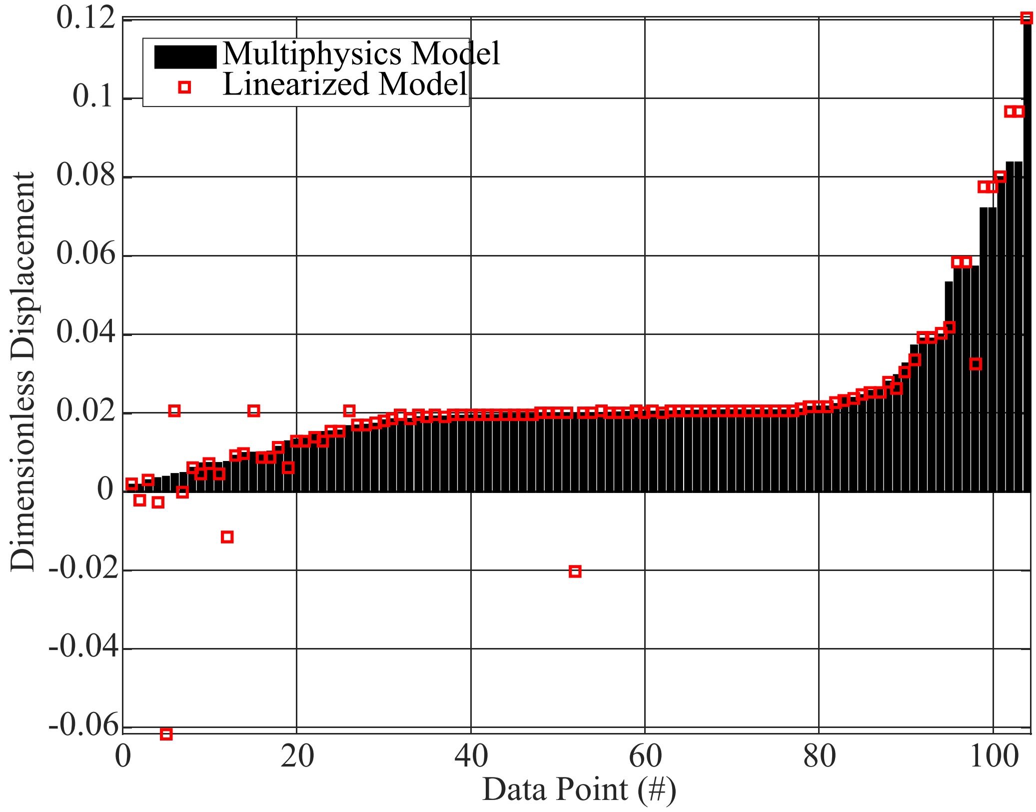

Figure 26. Bar graph of linearized multiplicative dynamic actuator model.
The multiplicative model is linearized in a multivariant Taylor series fashion using the first partial derivatives obtained from AD methods.

$$\Pi_\Delta \approx \Pi_{\Delta,0} + \sum_{\Pi_i \in \{\Pi\}} \left. \frac{\partial \Pi_\Delta}{\partial \Pi_i} \right|_{\{\Pi\}_0} (\Pi_i - \Pi_{i,0}) \qquad (3.5)$$

wherein $\Pi_{i,0}$ is the fixed value of the dimensionless group and the set of these values is denoted by $\{\Pi\}_0$. Due to the nature of AD these partial derivatives exhibit no discretization error and are calculated to machine precision. Here the values of the partial derivatives are presented to five significant figures.

We find that the linearized model behaves reasonably well for most values near the point of linearization, but as the individual terms vary further from their origin value there is significant degradation, shown in figure 26. The linearized model and its construction about an arbitrary point using AD is an interesting avenue of analysis. Another reason for formulating these derivative components is to quantify the displacement behavior in the vicinity of the fixed values from a sensitivity perspective. We calculate the percentage change in the displacement in response to a change in each of the Π-groups. This gives us a better idea of the sensitivity of the displacement with respect to each Π-group than the partial derivative alone due to the vastly different orders of magnitude that the individual groups vary within. We can compute the percent

Table 6. Sensitivity of dynamic actuator amplitude with respect to each Π-group.

Expression	Percent change (%)	Expression	Percent change (%)
$\left\lvert\frac{\Pi_{1,0}}{\Pi_{\Delta,0}}\frac{\partial\Pi_\Delta}{\partial\Pi_1}\right\rvert$	4.3098×10^{-1}	$\left\lvert\frac{\Pi_{2,0}}{\Pi_{\Delta,0}}\frac{\partial\Pi_\Delta}{\partial\Pi_2}\right\rvert$	3.3123×10^{-2}
$\left\lvert\frac{\Pi_{3,0}}{\Pi_{\Delta,0}}\frac{\partial\Pi_\Delta}{\partial\Pi_3}\right\rvert$	$\mathbf{1.4057\times10^{0}}$	$\left\lvert\frac{\Pi_{4,0}}{\Pi_{\Delta,0}}\frac{\partial\Pi_\Delta}{\partial\Pi_4}\right\rvert$	$\mathbf{1.2054\times10^{0}}$
$\left\lvert\frac{\Pi_{6,0}}{\Pi_{\Delta,0}}\frac{\partial\Pi_\Delta}{\partial\Pi_6}\right\rvert$	$\mathbf{1.0000\times10^{0}}$	$\left\lvert\frac{\Pi_{7,0}}{\Pi_{\Delta,0}}\frac{\partial\Pi_\Delta}{\partial\Pi_7}\right\rvert$	$\mathbf{1.0000\times10^{0}}$
$\left\lvert\frac{\Pi_{9,0}}{\Pi_{\Delta,0}}\frac{\partial\Pi_\Delta}{\partial\Pi_9}\right\rvert$	3.5094×10^{-2}	$\left\lvert\frac{\Pi_{10,0}}{\Pi_{\Delta,0}}\frac{\partial\Pi_\Delta}{\partial\Pi_{10}}\right\rvert$	1.8000×10^{-1}
$\left\lvert\frac{\Pi_{11,0}}{\Pi_{\Delta,0}}\frac{\partial\Pi_\Delta}{\partial\Pi_{11}}\right\rvert$	8.3092×10^{-1}	$\left\lvert\frac{\Pi_{13,0}}{\Pi_{\Delta,0}}\frac{\partial\Pi_\Delta}{\partial\Pi_{13}}\right\rvert$	9.6433×10^{-1}
$\left\lvert\frac{\Pi_{15,0}}{\Pi_{\Delta,0}}\frac{\partial\Pi_\Delta}{\partial\Pi_{15}}\right\rvert$	9.6421×10^{-1}	$\left\lvert\frac{\Pi_{17,0}}{\Pi_{\Delta,0}}\frac{\partial\Pi_\Delta}{\partial\Pi_{17}}\right\rvert$	*4.9241×10^{-3}*

Table 7. Voltage sensor regression model for individual Π-groups.

Dimensionless group	Description of function form	Regression function
Π_1	Quadratic	$\beta_1\Pi_1^2+\beta_2\Pi_1+\beta_3$
Π_2	Linear-to-Log w/Logistic Transition	$\beta_6\Pi_2+\beta_7+\frac{\beta_3+\beta_4\log(\Pi_2+\beta_5)-\beta_6\Pi_2-\beta_7}{1+\exp(-\beta_1(\Pi_2-\beta_2))}$
Π_3	Quadratic	$\beta_1\Pi_3^2+\beta_2\Pi_3+\beta_3$
Π_4	Quadratic	$\beta_1\Pi_4^2+\beta_2\Pi_4+\beta_3$
Π_5	Linear	$\beta_1\Pi_5$
Π_6	Decaying Monomial	β_1/Π_6
Π_{10}	Monomial w/Root	$\beta_1(1/2-\Pi_{10})^{\beta_2}+\beta_3$
Π_{13}	Decaying Rational	$(\beta_3\Pi_{13}+\beta_4)/(\beta_1\Pi_{13}^2+\beta_2\Pi_{13}+1)$
Π_{15}	Single Pole w/Sym.	$\beta_1/\lvert\Pi_{15}\rvert$
Π_{17}	Decaying Rational	$(\beta_3\Pi_{17}+\beta_4)/(\beta_1\Pi_{17}^2+\beta_2\Pi_{17}+1)$
Π_{18}	Linear	$\beta_1\Pi_{18}$
Π_{19}	Linear w/Quad Pole	$\beta_1\Pi_{19}+\beta_2/\Pi_{19}^2+\beta_3$

change in displacement in response to a 1% change in a given dimensionless group Π_i as:

$$\left\lvert\frac{\Pi_\Delta-\Pi_{\Delta,0}}{\Pi_{\Delta,0}}\right\rvert 100 := \left\lvert\frac{\Pi_{i,0}}{\Pi_{\Delta,0}}\frac{\partial\Pi_\Delta}{\partial\Pi_i}\right\rvert. \tag{3.6}$$

From the results provided in table 6 we can see that at the point of linearization the dynamic actuator displacement is most sensitive (**bold**) to the Ionic Fraction, Solvent Size, Aspect Ratio, and Driving Potential and least sensitive (*italicized*) to the Resistive Dynamics. This follows our current understanding of IPMC actuation, where the solvent and mobile ionic species have significant impact on the performance of these materials [30–32]. This encourages future research endeavors into the optimization of this solvent-ion paring to obtain high-performance IPMC actuators in dynamic applications.

3.3. Regression model for the dynamic voltage response

We perform the same analysis for the dynamic open-circuit voltage response for the IPMC, again formulating a set of presumptive functional form to regress the amplitude results obtained from the multiphysics model. These one-dimensional regression models, provided in table 7, are then used to formulate the multiplicative decomposition model which is tested against the concatenated data of our parametric studies.

We formulate the multiplicative model shown in equation (3.7), which also features a reduced number of regression coefficients due to the normalization of the individual models

$$\begin{aligned}\Pi_\phi = {} & \beta_0\frac{\Pi_5\Pi_{18}}{\Pi_6\lvert\Pi_{15}\rvert}\left(1+\beta_2\Pi_1+\beta_1\Pi_1^2\right)\\ & \times\left(1+\beta_8\Pi_2\frac{\beta_5+\beta_6\log(\Pi_2+\beta_7)-1-\beta_8\Pi_2}{1+\exp(-\beta_3(\Pi_2-\beta_4))}\right)\\ & \times\left(1+\beta_{10}\Pi_3+\beta_9\Pi_3^2\right)\left(1+\beta_{12}\Pi_4+\beta_{11}\Pi_4^2\right)\\ & \times\left(1+\beta_{13}\left(\frac{1}{2}-\Pi_{10}\right)^{\beta_{14}}\right)\frac{1+\beta_{17}\Pi_{13}}{1+\beta_{16}\Pi_{13}+\beta_{15}\Pi_{13}^2}\\ & \times\frac{1+\beta_{20}\Pi_{17}}{1+\beta_{19}\Pi_{17}+\beta_{18}\Pi_{17}^2}\left(1+\beta_{21}\Pi_{19}+\frac{\beta_{22}}{\Pi_{19}^2}\right).\end{aligned} \tag{3.7}$$

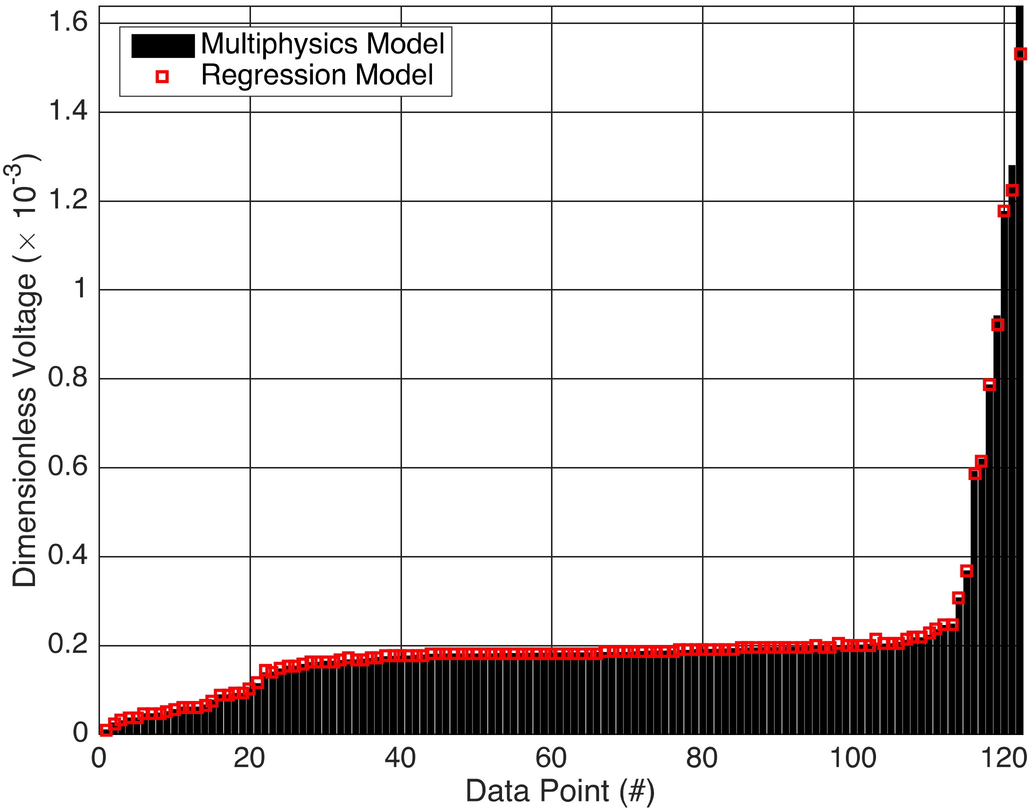

Figure 27. Bar graph of multiplicative dynamic voltage sensor model performance. The individual regression models are combined multiplicatively to obtain a single model for the dynamic voltage sensor response. The above graph demonstrates the capability of this subproblem to multiplicative decomposition approach for high-dimensional regression modeling.

As before, we find the multiplicative decomposition is able to capture the transduction behavior of the multiphysics model with great accuracy (shown in figure 27). Here we obtain the r^2 and adjusted-r^2 as: $r^2 = 0.99749$ and $r^2_{\mathrm{adj}} = 0.99690$. The above results do exhibit some error, specifically in the largest values for sensing voltage. A more in-depth investigation reveals the data points in question are those in which the displacement amplitude is the driving Π-group, and the errors were not found in the initial one-dimensional model corresponding to the Driving Displacement. This indicates that while the current multiplicative decomposition approach is a powerful tool for formulating high-dimensional models for IPMC transduction, more work is necessary to formulate a robust model that is capable of correcting for errors that are introduced in the process.

As before AD methods are leveraged to formulate a linearization about fixed values for the Π-groups, and the linearized dynamic voltage response is computed as shown in (3.8) wherein the necessary derivative terms from AD are provided in table 8

$$\Pi_\phi \approx \Pi_{\phi,0} + \sum_{\Pi_i \in \{\Pi\}} \left.\frac{\partial \Pi_\phi}{\partial \Pi_i}\right|_{\{\Pi\}_0} (\Pi_i - \Pi_{i,0}). \tag{3.8}$$

This linearized model shows similar performance when compared to the nonlinear multiplicative model (provided in figure 28). As with the actuator model, the computation of the partial derivatives is primarily done in order to conduct a kind of sensitivity analysis for the multiplicative model. Observing the change in the multiplicative model to a 1% change in each of its independent parameters using the derivatives obtained by AD, we find the sensitivity results in table 9.

Table 8. First partial derivatives for multiplicative dynamic voltage sensor model.

Partial derivative	Value	Partial derivative	Value
$\frac{\partial \Pi_\phi}{\partial \Pi_1}$	2.6998×10^{-6}	$\frac{\partial \Pi_\phi}{\partial \Pi_2}$	8.7715×10^{-9}
$\frac{\partial \Pi_\phi}{\partial \Pi_3}$	2.1401×10^{-3}	$\frac{\partial \Pi_\phi}{\partial \Pi_4}$	2.4250×10^{-5}
$\frac{\partial \Pi_\phi}{\partial \Pi_5}$	1.0220×10^{-4}	$\frac{\partial \Pi_\phi}{\partial \Pi_6}$	-1.1498×10^{-6}
$\frac{\partial \Pi_\phi}{\partial \Pi_{10}}$	1.2958×10^{-4}	$\frac{\partial \Pi_\phi}{\partial \Pi_{13}}$	-7.2861×10^{-9}
$\frac{\partial \Pi_\phi}{\partial \Pi_{15}}$	-1.8397×10^{-4}	$\frac{\partial \Pi_\phi}{\partial \Pi_{17}}$	4.1421×10^{4}
$\frac{\partial \Pi_\phi}{\partial \Pi_{18}}$	6.1322×10^{-3}	$\frac{\partial \Pi_\phi}{\partial \Pi_{19}}$	2.0932×10^{-7}

We find the model to be equally sensitive to a large number of Π-groups; the Hydraulic Number, Aspect Ratio, Mobile Charge Number, and Driving Displacement all feature 1% sensitivity to changes in these parameters while the remaining dimensionless groups are of an order of magnitude or more

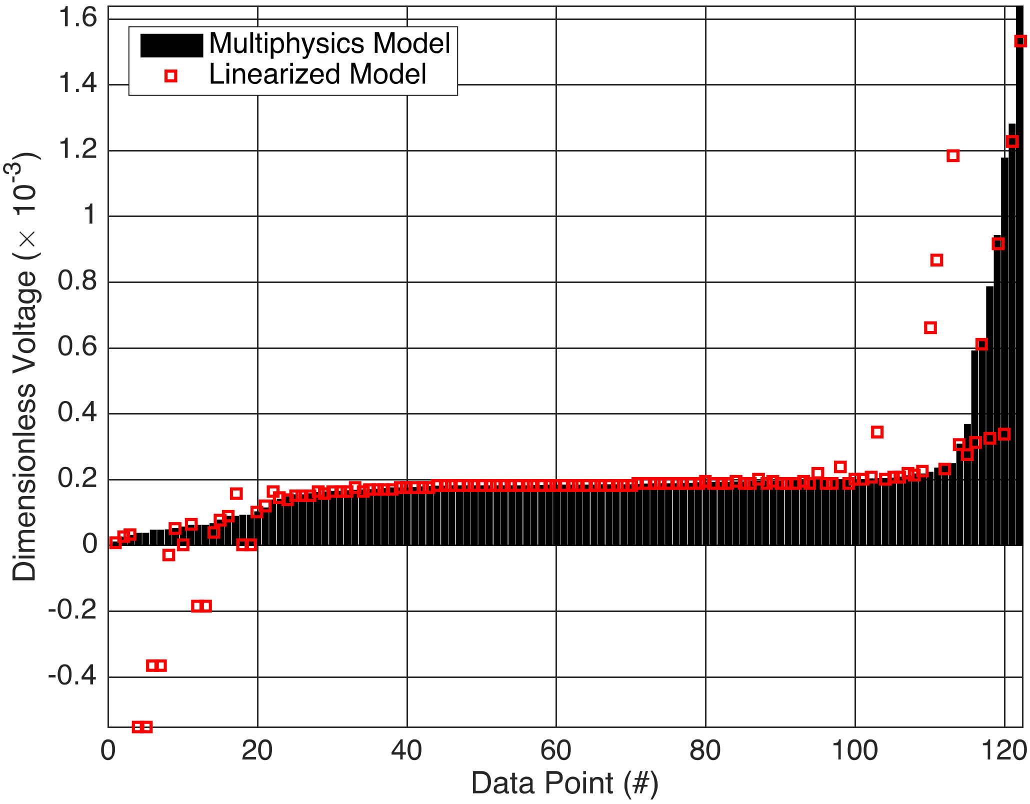

Figure 28. Bar graph of linearized multiplicative dynamic voltage sensor model. The multiplicative model is linearized in a multivariant Taylor series fashion using the first partial derivatives obtained from AD methods.

Table 9. Sensitivity of dynamic voltage sensor response with respect to each Π-group.

Expression	Percent change (%)	Expression	Percent change (%)
$\left\lvert \frac{\Pi_{1,0}}{\Pi_{\phi,0}} \frac{\partial \Pi_\phi}{\partial \Pi_1} \right\rvert$	1.8018×10^{-1}	$\left\lvert \frac{\Pi_{2,0}}{\Pi_{\phi,0}} \frac{\partial \Pi_\phi}{\partial \Pi_2} \right\rvert$	3.3376×10^{-3}
$\left\lvert \frac{\Pi_{3,0}}{\Pi_{\phi,0}} \frac{\partial \Pi_\phi}{\partial \Pi_3} \right\rvert$	1.9490×10^{-1}	$\left\lvert \frac{\Pi_{4,0}}{\Pi_{\phi,0}} \frac{\partial \Pi_\phi}{\partial \Pi_4} \right\rvert$	1.8312×10^{-1}
$\left\lvert \frac{\Pi_{5,0}}{\Pi_{\phi,0}} \frac{\partial \Pi_\phi}{\partial \Pi_5} \right\rvert$	$\mathbf{1.0000 \times 10^{0}}$	$\left\lvert \frac{\Pi_{6,0}}{\Pi_{\phi,0}} \frac{\partial \Pi_\phi}{\partial \Pi_6} \right\rvert$	$\mathbf{1.0000 \times 10^{0}}$
$\left\lvert \frac{\Pi_{10,0}}{\Pi_{\phi,0}} \frac{\partial \Pi_\phi}{\partial \Pi_{10}} \right\rvert$	3.1698×10^{-1}	$\left\lvert \frac{\Pi_{13,0}}{\Pi_{\phi,0}} \frac{\partial \Pi_\phi}{\partial \Pi_{13}} \right\rvert$	1.2377×10^{-1}
$\left\lvert \frac{\Pi_{15,0}}{\Pi_{\Delta,0}} \frac{\partial \Pi_\phi}{\partial \Pi_{15}} \right\rvert$	$\mathbf{1.0000 \times 10^{0}}$	$\left\lvert \frac{\Pi_{17,0}}{\Pi_{\phi,0}} \frac{\partial \Pi_\phi}{\partial \Pi_{17}} \right\rvert$	1.6211×10^{-3}
$\left\lvert \frac{\Pi_{18,0}}{\Pi_{\phi,0}} \frac{\partial \Pi_\phi}{\partial \Pi_{18}} \right\rvert$	$\mathbf{1.0000 \times 10^{0}}$	$\left\lvert \frac{\Pi_{19,0}}{\Pi_{\phi,0}} \frac{\partial \Pi_\phi}{\partial \Pi_{19}} \right\rvert$	2.5808×10^{-1}

less sensitive. These results fall in-line with our previous discussion regarding the open-circuit voltage transduction response. The Hydraulic Number exhibits a large sensitivity due to IPMC mechanoelectrical transduction being driving primarily by advective transport of the mobile ionic species. The advective ionic redistribution induced by the Driving Displacement, and for a given level of displacement the Mobile Charge Number characterizes the amount of charge accumulation at the polymer-electrode interface where the sensing potential is established.

4. Evaluating the predictive capabilities of the new regression models

As a final objective we seek to evaluate the capability of the regression models, equations (3.3) and (3.7), to predict IPMCs in experimental settings. To this end, we take samples of IPMCs fabricated in-lab and collect data on their dynamic actuator displacement and voltage response and use the multiplicative regression models to fit the data. The regression models feature a great number of independent parameters (the Π-groups), not all of which are conveniently determined or even controllable when fabricating IPMCs in-lab. For this reason, typical experimental setups are only capable of manipulating a subset of the independent parameters that have been used in this model, which will be elaborated on for the actuator and sensor experiments in the next sections.

4.1. Experimental setup

4.1.1. Dynamic cantilever actuator. To characterize the IPMCs dynamic actuation response we use a laser displacement sensor (Micro-Epsilon optoNCDT-1401) to monitor tip deflection. A sinusoidal signal of known amplitude and frequency is applied to the clamp electrodes in parallel with the IPMC and DAQ (Keithley DAQ6510) using a function

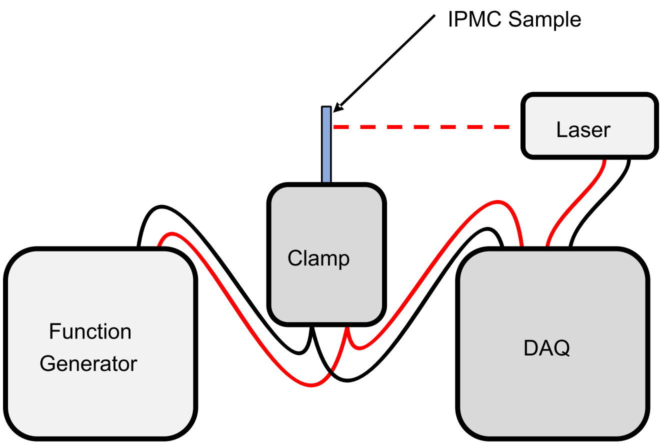

Figure 29. Illustration of dynamic IPMC actuator experimental setup.
The dynamic actuator amplitude is captured using a laser displacement sensor. The input voltage to the IPMC clamps is fed into the DAQ along with the laser displacement reads using a solid-state multiplexer for high capture rate.

generator (SIGLENT SDG1025). The displacement readings as well as the applied voltage are logged in the DAQ using the 7710 solid-state Multiplexer (MUX) module card to achieve a high data capture rate. An illustration of this experimental setup is provided in figure 29.

By capturing the input and output simultaneously we can process the data together and formulate the necessary dimensionless groups for our analysis. In the case of the dynamic actuator, we are able to control the input voltage, input frequency, and IPMC free length. This allows us to formulate/control the Driving Potential, Driving Frequency, and Aspect Ratio for our dimensionless model. Note though that the Driving Frequency is the product of the input frequency and the diffusion timescale, and without knowledge of the ionic diffusivity we are unable to fully nondimensionalize the experimental results. Thankfully, we can formulate a mixed dimensional/dimensionless regression model that leaves the regression coefficients multiplying the input frequency as dimensional and the unknown diffusion will simply be encoded into the regression coefficient.

The experimental data recorded in the DAQ is processed through the same DFT algorithm that the dynamic multiphysics model results were processed with, which extracts the amplitude and frequency of the signal across. This data is then nondimensionalized using the known free length, membrane thickness, and thermal voltage. The dimensionless data is binned according to a set of scaling and rounding operations. During the nondimensionalization of the data it is possible that two different combinations of free length and displacement amplitude result in a dimensionless displacement that are close enough to be binned together. This is done because during the nondimensionalization process it is possible for some data points to nondimensionalize into values that are close enough to be considered effectively the same value. The bins collect these occurrences, and once the data is binned the amplitude and frequency results in each bin are averaged.

4.1.2. Dynamic open-circuit voltage. To characterize the IPMCs dynamic voltage response we use a very similar setup as for actuation. The laser displacement sensor is used to monitor tip deflection, which is driven using a dynamic shaker (Vibration Research VR-5200 shaker, Labworks Inc. pa-138 amplifier). The shaker is controlled via PC using an attached accelerometer for feedback (Vibration Research VR-8500 Control System) and is calibrated beforehand for the IPMC load. The clamp electrodes are connected to the DAQ along with the laser displacement and logged using the MUX card to achieve a high data capture rate. Again, an illustration of sensor experimental setup is provided in figure 30.

Like in the case of the dynamic actuator, we are able to control the input voltage, input displacement amplitude, and IPMC free length. This allows us to formulate/control the Driving Displacement, Driving Frequency, and Aspect Ratio for our dimensionless model. Again, without the diffusion timescale we are unable to fully nondimensionalize the experimental results. We similarly formulate a mixed dimensional/dimensionless regression model that leaves the regression coefficients multiplying the input frequency as dimensional and hence account for the unknown diffusion timescale. The experimental data recorded in the DAQ is again processed through the DFT, nondimensionalized, binned, and averaged. In both actuation and sensing experiments the IPMC samples are rehydrated between each trial capture.

4.2. Modeling experimental data using computational regression results

4.2.1. Actuator model. The multiplicative decomposition for dynamic actuators indicates that we may formulate a suitable regression model for this type of experiment as shown below. The parameter β_0 collects the effects of all other Π-groups that are unaccounted for in the experiment. A detailed material characterization of the IPMC sample may provide insight into the values of these Π-groups, but ultimately without the capability to vary these properties within a single sample throughout the course of an experiment there is no need to include them in a multiplicative regression model

$$\Pi_\Delta = \beta_0 \Pi_6 \left|\Pi_7\right| \left(\frac{\beta_1}{\log\left(1+\beta_2^* \omega\right)+\beta_3} + 1 \right). \tag{4.1}$$

The superscripted * indicates that the regression coefficient is dimensional, and hence does not directly equate with the corresponding coefficient in the previous analysis of section 3.2. The experimental results for our actuation are obtained by varying the free length, applied voltage, and frequency of sinusoidal waveform. We present the results of the experiments after nondimensionalization along with the regression model after the '*nlinfit*' routine was applied. The nonlinear fitting used the same settings as for the earlier regression analysis. The experimental data is plotted along with 1 standard deviation in order to better understand the accuracy of the regression model and is presented from four viewpoints to aid in visualizing the data and fit.

The regression model fits the variations in experimental data well, demonstrated in figure 31. We look to further

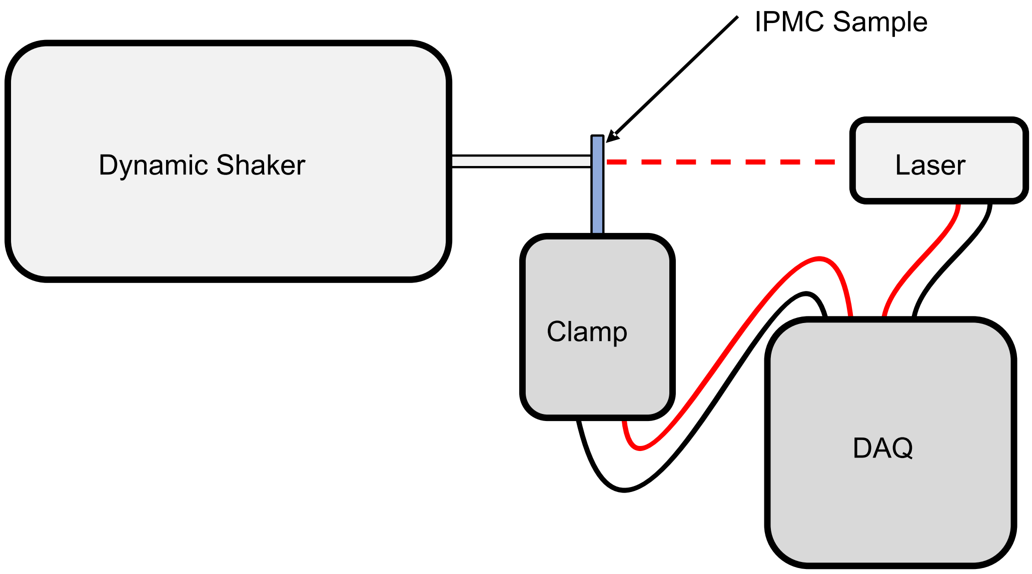

Figure 30. Illustration of dynamic IPMC voltage sensor experimental setup.
The dynamic voltage sensor response is captured using the DAQ. The input displacement to the IPMC tip via a dynamic shaker is recorded with the laser displacement sensor and fed into the DAQ along with clamp voltage using a solid-state multiplexer for high capture rate.

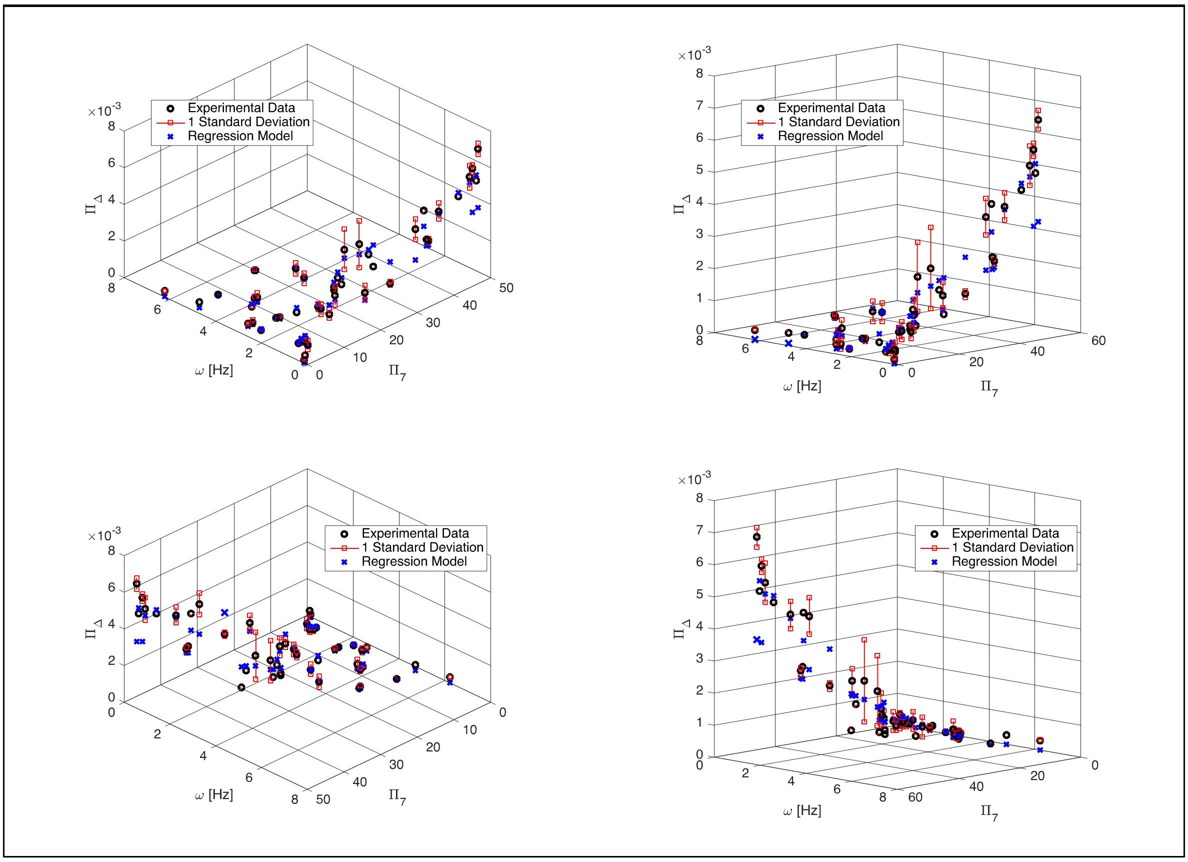

Figure 31. Multiplot of actuator experiment results.
The dynamic actuator amplitude as captured from the experimental setup is plotted along with the regression modeling results for the same data. The experimental data is collected over many trials and nondimensionalized, then binned and averaged. In the plot the averaged data is plotted with bars of 1 standard deviation.

quantify the fit by analyzing how well the regression model can predict values that would be reasonably expected to occur within the experimental data. To formulate a metric for this, we calculate the percentage of regression model points which fall within three standard deviations of the experimental averages, where nearly all of the experimental data would be expected

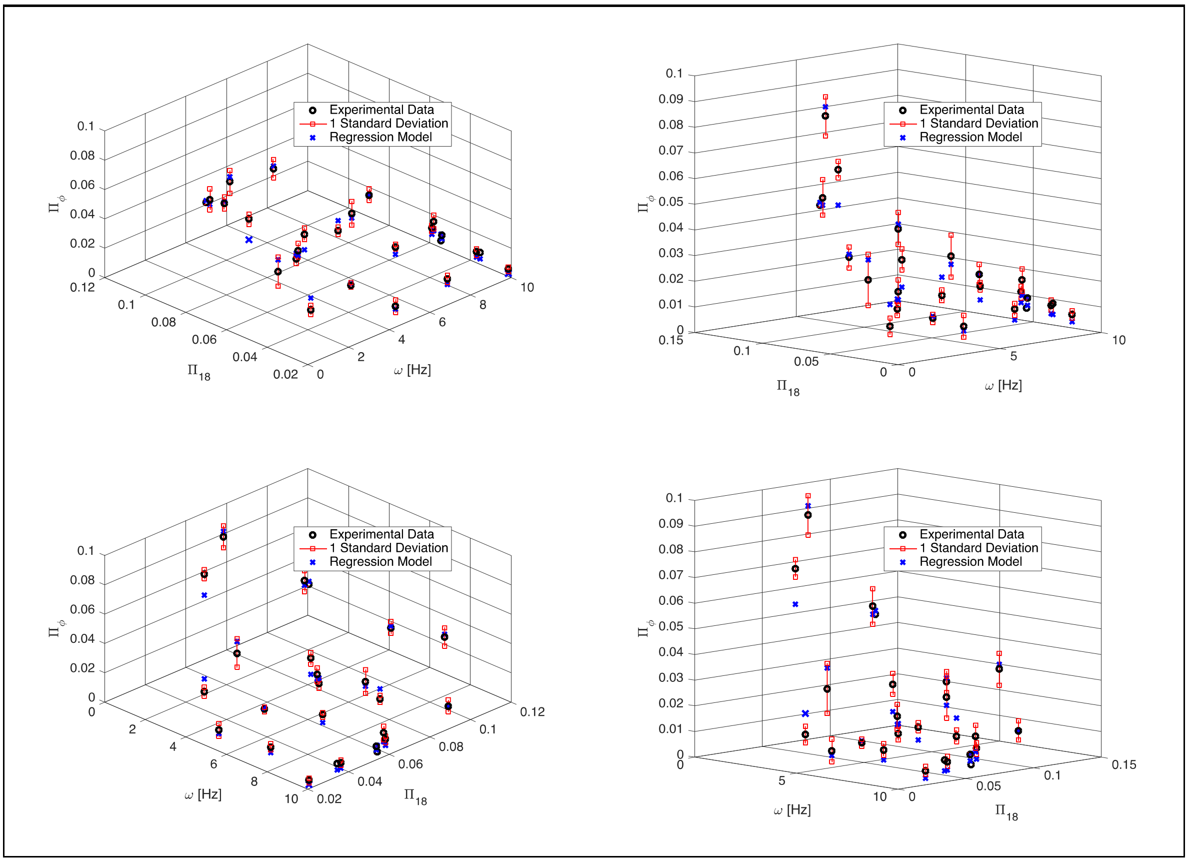

Figure 32. Multiplot of voltage sensor experiment results.
The dynamic voltage sensor response as captured from the experimental setup is plotted along with the regression modeling results for the same data. The experimental data is collected over many trials and nondimensionalized, then binned and averaged. In the plot the averaged data is plotted with bars of 1 standard deviation.

to reside. There are some experimental data points which have only one sample in the corresponding bin and hence zero standard devotion but removing these the regression model is capable of predicting 75.9% of the data within three standard deviation of experimental averages. We also find that most of the error resides at the higher end of the Driving Voltage, and hence indicates that the model may be failing to capture the nonlinear behavior in relation to the applied voltage that was not present in the multiphysics model. The calculated r^2 and adjusted-r^2 are 0.83244 and 0.82047, respectively.

4.2.2. Sensor model. For the sensor model we proceed in nearly identical steps. With the dimensionless groups we are able to influence with the experimental setup we can reasonably predict the following regression model, obtained from the multiplicative model in section 3.3

$$\Pi_\phi = \beta_0 \frac{\Pi_{18}}{\Pi_6} \frac{\beta_1^* \omega + 1}{\beta_2^* \omega^2 + \beta_3^* \omega + 1}. \tag{4.2}$$

The superscripted * again indicates that the regression coefficient is dimensional, and hence does not directly equate with the corresponding coefficient in the previous analysis of section 3.3. For our sensor experiments we vary the free length, displacement amplitude voltage, and frequency of sinusoidal waveform. We present the results of the experiments after nondimensionalization along with the regression model after the '*nlinfit'* routine was applied. The experimental data and model are similarly presented from four viewpoints to aid in visualizing the data and fit.

Again, we find that the regression model fits the variations in experimental data well (see figure 32). Removing any data points which have only one sample in the corresponding bin we find that the regression model is capable of predicting 85.7% of the data within three standard deviation of experimental averages. Here most of the error resides in the low frequency data, with these experimental values having a broader distribution that is attributed to the dynamic shaker not tracking the desired displacement profile for these slower speeds. The calculated r^2 and adjusted-r^2 are 0.93700 and 0.92440, respectively.

5. Conclusion

In this work we have leveraged a new multiphysics modeling framework which accounts for the coupled solvent/ion transport to characterized IPMC transduction phenomena. Using a nondimensionalized set of governing equations, we have extensively explored and characterized the dimensionless transduction response for IPMC actuators and sensors under static and dynamic loading. During this analysis we have uncovered and described the counterintuitive effects of the Maxwell Number and Osmotic Number on the actuator response and their relation to boundary layer formation via the Reciprocal Double Layer.

The dynamic actuation and voltage response were further characterized using nonlinear regression models for the individual Π-group variations. These univariant regression models were combined under an assumption of multiplicative decomposition of the multivariant response. These multiplicative models showed great performance when compared to the multiphysics model. Using the technique of AD these nonlinear models were linearized and the partial derivatives obtained were used to formulate sensitivities of the transduction response with respect to each of the pertinent Π-groups.

Additionally, we presented a powerful new approach to characterizing IPMC actuators and sensors. The hybrid computational-experimental regression modeling allows for complex nonlinear regression models to be discovered using numerical experiments and used for interpreting physical experiments and IPMC samples. The regression models developed on the computational results demonstrated great performance, which indicates that these models developed in the computational domain can serve as models for interpreting real-world experimental results. Some final remarks on the presented model. The underlying multiphysics framework is based on an infinitesimal strain formulation with a linear elastic material model. For this reason, the preceding analysis must be taken with an understanding that the large deformations observed are calculated under the infinitesimal strain formulation and hence incur a degree of error. This relates to our discussion on the errors in the experimental analysis for dynamic actuation, in that the dimensionless groups which exhibited the most error was for large values of the Driving Potential Π_7. The current model begins to degrade from a fully nonlinear model for deformations in the range of $\Pi_\triangle \approx 0.3$, or a displacement equal to 30% of the actuator length. Furthermore, the regression models obtained from the computational multiphysics results were formulated in a time-dependent model. The frequency response extracted from this model may not fully account for the frequency response and any resonant frequencies in the mechanical model. An extension of this work to cast the dimensionless formulation into a nondimensional frequency domain may be capable of extracting such resonant responses for the actuator displacement, blocking force, short-circuit current, and open-circuit voltage.

Acknowledgments

The authors acknowledge the partial financial support from the US National Science Foundation (NSF), Partnerships for International Research and Education (PIRE) Program, Grant No. 1545857. Any opinions, findings and conclusions or recommendations expressed in this material are those of the author(s) and do not necessarily reflect the views of the NSF.

Data availability statement

The data that support the findings of this study are available upon reasonable request from the authors.

ORCID iDs

Zakai J Olsen https://orcid.org/0000-0002-4499-6677
Kwang J Kim https://orcid.org/0000-0003-2134-4964

References

[1] Bar-Cohen Y 2002 Electroactive polymers as artificial muscles: a review *J. Spacecr. Rockets* **39** 822–7

[2] Hines L, Petersen K, Lum G Z and Sitti M 2017 Soft actuators for small-scale robotics *Adv. Mater.* **29** 1603483

[3] Shahinpoor M, Bar-Cohen Y, Simpson J O and Smith J 1998 Ionic polymer-metal composites (IPMCs) as biomimetic sensors, actuators and artificial muscles—a review *Smart Mater. Struct.* **7** R15–R30

[4] Kim K J, Yim W, Paquette J W and Kim D 2007 Ionic polymer-metal composites for underwater operation *J. Intell. Mater. Syst. Struct.* **18** 123–31

[5] Shahinpoor M 1992 Conceptual design, kinematics and dynamics of swimming robotic structures using ionic polymeric gel muscles *Smart Mater. Struct.* **1** 91–94

[6] Yim W, Lee J and Kim K J 2007 An artificial muscle actuator for biomimetic underwater propulsors *Bioinspir. Biomim.* **2** S31–S41

[7] Shahinpoor M and Kim K J 2001 Ionic polymer-metal composites: I. Fundamentals *Smart Mater. Struct.* **10** 819–33

[8] Kim K J and Shahinpoor M 2003 Ionic polymer-metal composites: II. manufacturing techniques *Smart Mater. Struct.* **12** 65–79

[9] Shahinpoor M and Kim K J 2004 Ionic polymer-metal composites: III. Modeling and simulation as biomimetic sensors, actuators, transducers, and artificial muscles *Smart Mater. Struct.* **13** 1362–88

[10] Shahinpoor M and Kim K J 2005 Ionic polymer-metal composites: IV. Industrial and medical applications *Smart Mater. Struct.* **14** 197–214

[11] Jo C, Pugal D, Oh I K, Kim K J and Asaka K 2013 Recent advances in ionic polymer-metal composite actuators and their modeling and applications *Prog. Polym. Sci.* **38** 1037–66

[12] Tiwari R and Garcia E 2011 The state of understanding of ionic polymer metal composite architecture: a review *Smart Mater. Struct.* **20** 083001

[13] Olsen Z J, Kim K J and Oh I 2020 Developing next generation ionic polymer-metal composite materials: perspectives for enabling robotics and biomimetics *Polym. Int.* **70** 7–9

[14] Olsen Z J and Kim K J 2021 A hyperelastic porous media framework for ionic polymer-metal composite actuators and sensors: thermodynamically consistent formulation and nondimensionalization of the field equations *Smart Mater. Struct.* **30** 095024

[15] Slattery J C, Sagis L and Oh E-S 2007 *Interfacial Transport Phenomena* (Boston, MA: Springer US)

[16] Aris R 1962 *Vectors, Tensors and the Basic Equations of Fluid Mechanics* (New York, NY: Dover Publications Inc)

[17] McConnell A J 1957 *Applications of Tensor Analysis* (New York, NY: Dover Publications Inc)

[18] Wallmersperger T, Akle B J, Leo D J and Kröplin B 2008 Electrochemical response in ionic polymer transducers: an experimental and theoretical study *Compos. Sci. Technol.* **68** 1173–80
[19] Nemat-Nasser S and Li J Y 2000 Electromechanical response of ionic polymer-metal composites *J. Appl. Phys.* **87** 3321–31
[20] Porfiri M, Leronni A and Bardella L 2017 An alternative explanation of back-relaxation in ionic polymer metal composites *Extreme Mech. Lett.* **13** 78–83
[21] Porfiri M, Sharghi H and Zhang P 2018 Modeling back-relaxation in ionic polymer metal composites: the role of steric effects and composite layers *J. Appl. Phys.* **123** 014901
[22] Porfiri M 2008 Charge dynamics in ionic polymer metal composites *J. Appl. Phys.* **104** 104915
[23] Cha Y and Porfiri M 2014 Mechanics and electrochemistry of ionic polymer metal composites *J. Mech. Phys. Solids* **71** 156–78
[24] Volpini V, Bardella L, Rodella A, Cha Y and Porfiri M 2017 Modelling compression sensing in ionic polymer metal composites *Smart Mater. Struct.* **26** 035030
[25] Volpini V and Bardella L 2021 Asymptotic analysis of compression sensing in ionic polymer metal composites: the role of interphase regions with variable properties *Math. Eng.* **3** 1–31
[26] Pugal D 2012 *Physics Based Model of Ionic Polymer-Metal Composite Electromechanical and Mechanoelectrical Transduction* (Reno: University of Nevada)
[27] Searson D P 2015 GPTIPS 2: an open-source software platform for symbolic data mining *Handbook of Genetic Programming Applications* (Cham: Springer International Publishing) pp 551–73
[28] Verma A 2000 An introduction to automatic differentation *Curr. Sci.* **78** 804–7
[29] Neidinger R D 2010 Introduction to automatic differentiation and MATLAB object-oriented programming *SIAM Rev.* **52** 545–63
[30] Nemat-Nasser S and Wu Y 2003 Comparative experimental study of ionic polymer-metal composites with different backbone ionomers and in various cation forms *J. Appl. Phys.* **93** 5255–67
[31] Nemat-Nasser S, Zamani S and Tor Y 2006 Effect of solvents on the chemical and physical properties of ionic polymer-metal composites *J. Appl. Phys.* **99** 104902
[32] Nemat-Nasser S and Zamani S 2006 Modeling of electrochemomechanical response of ionic polymer-metal composites with various solvents *J. Appl. Phys.* **100** 064310